Investigating structural covariance of the white matter tract and cortical area in the visual system of living human brains

（ヒト生体脳視覚系における白質線維束と皮質領域の構造的共分散の検討）

Toshikazu Miyata

Graduate School of Frontier Biosciences
Osaka University

March 2023

Abstract

Vision is an essential sensory modality for humans and animals for survival. Neuroscientists have investigated neural mechanisms of visual processing by investigating anatomy, functional organization and response properties of the visual system. Still, questions remain why there are individual differences in the human visual system. Individual differences in the human visual system exist at many scales, spanning gene expression, white matter tissue properties, and the size and shape of cortical areas.

One notable example is an approximately 3-fold range in the size of the human primary visual cortex (V1), a much larger range than is found in overall brain size. A previous study reported a correlation between optic tract (OT) cross-section area and V1 size in post-mortem human brains, suggesting that there may be a common developmental mechanism for multiple components of the human visual pathways. However, it is not yet clear how much findings on such structural covariance in post-mortem human brains is generalizable to living human brains or not and what types of factors may influence such structural covariance.

For the last decades, the advancement of the non-invasive measurement by using magnetic resonance imaging (MRI) has made it possible to measure functional and structural properties in living human brains.

In this dissertation, I evaluated the relationship between properties of the OT and V1 in a much larger sample of living human brains by analyzing the Human Connectome Project (HCP) 7 Tesla Retinotopy Dataset, which is currently the largest available dataset including retinotopic mapping data measured with functional MRI (fMRI) and white matter tract data measured with diffusion MRI (dMRI). I found a negative correlation between OT property (fractional anisotropy) and V1 size. This correlation, though small, was consistent across multiple dMRI datasets differing in acquisition parameters. Further, I found that both V1 size and OT properties were correlated among twins, with higher correlations for monozygotic than dizygotic twins, indicating a high degree of heritability for both properties. Together, these results demonstrate covariation across individuals in properties derived from the retina (OT) and visual cortex (V1) and show that each is influenced by genetic factors.

Table of Contents

Chapter 1. General introduction of the human visual system and brain imaging

1.1 Structure of the human brain and visual pathway

1.1.1 The organization of the human cerebrum

Vision is an essential sensory modality for humans and animals to receive various information from the environment and make actions. Understanding of the visual system in the human brain is very important to reveal the underlying neurobiological mechanisms supporting daily-life experiences and to understand visual disorders. Hereafter, I will review background information of the human brain which is necessary to understand the focus of this dissertation, to understand the relationship between visual white matter tract and cortical visual area.

Broadly speaking, the human brain consists of the cerebrum, cerebellum, and brainstem. While the cerebellum involves maintaining the body's balance, the brainstem involves controlling involuntary functions such as respiration and circulation, and relaying sensory and motor signals (Purves et al., 2008). In contrast, the cerebrum is composed of a number of cortical areas supporting different types of information processing and fiber pathways connecting between them. While major visual areas and fiber pathways related to visual processing have been identified (Wandell & Winawer, 2011), there are yet many remaining questions about the visual system in the cerebrum, including a question about individual differences of the cortical visual area, which will be addressed in this dissertation.

The cerebrum consists of two major tissue structures; gray matter and white matter (Figure 1.1; Fields, 2008). The gray matter is located on the surface of the cerebrum (cerebral cortex) and consists of the neuron cell bodies, whose electrical response is considered as neural activity. On the other hand, the white matter is mostly composed of myelinated nerve fibers (axons) and plays a role in carrying signals between brain regions. Many neuroscience studies focus on understanding the functional response of the cortical regions by measuring neuronal activity in gray matter (Bullock et al., 2005), while white matter studies focus on neural connectivity of each region by using post-mortem human brains and animal brains (Rockland, 2020). Some studies have discussed how white matter lesions affect perception and cognition by investigating post-mortem human brains (Catani & Ffytche, 2005). However, there were large gaps due to the different approaches between measurement of functional and anatomical studies.

In this dissertation, I aim to investigate how properties of the regions in gray matter, such as the primary visual cortex (V1), are related to properties of white matter pathways carrying signals to that region. This will give us an insight on how these two major structures (gray matter and white matter) may be mutually affecting each other and maturing during the development. To understand the relationship between gray matter

and white matter, I studied the visual system not only because the visual system plays an important role in our daily lives, but also it is one of the widely studied systems in systems neuroscience and the functional organization and anatomy is relatively well understood (Livingstone & Hubel, 1988). Therefore, the visual system is a suitable system to address questions about the relationship between gray matter and white matter, since it is relatively well known which white matter tract carries signals to which cortical area (Rokem et al., 2017). In the next subchapter, I will make a review on existing literature on the human visual system, including findings from non-human primates' visual system.

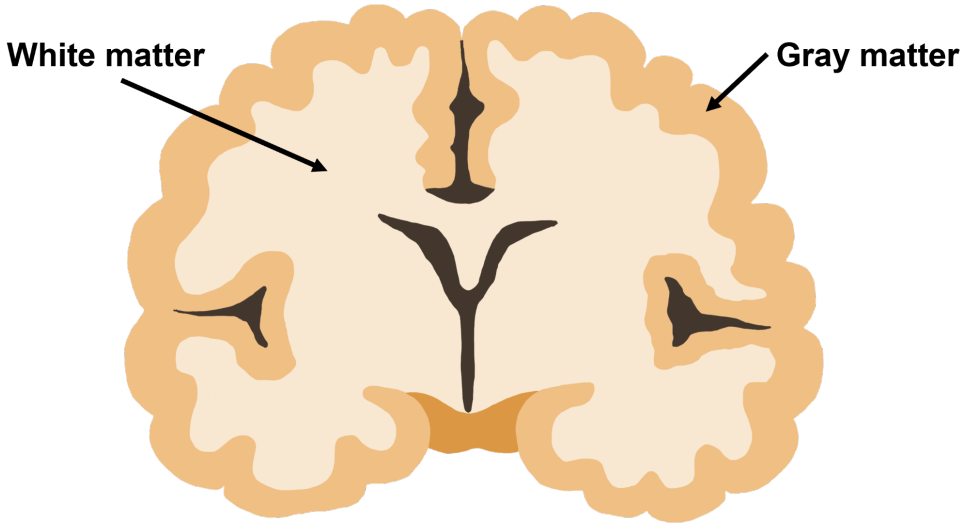

Figure 1.1. Schematic illustration of gray matter and white matter in the human cerebrum. The gray matter is located on the surface of the cerebrum and consists of the cell bodies of neurons. In contrast, the white matter consists of myelinated axons and located in the deep area of the cerebrum.

1.1.2 The literature on the organization of the primate visual system

Organization of major neural pathways in the early visual processing

Figure 1.2 depicts the schematic representation of the visual pathways in the human brain. The visual information in the environment (light) is first received by cells in the retina. The retina is composed of different types of cells, including the photoreceptor receiving visual information and retinal ganglion cells (RGCs), which is a neuron sending signals to subsequent visual areas (Wässle & Boycott, 1991). RGCs contain axons carrying signals to later visual areas and those axons consist of white matter tracts, the optic nerve and optic tract (OT). The optic nerve is a white matter tract, which is composed of axons from RGCs in each eye to the optic chiasm. In the optic chiasm, axons from the temporal retina do not cross the midline whereas axons from the nasal retina cross. A group of axons posterior to the optic chiasm is the OT, which conveys visual information from the optic chiasm to the lateral geniculate nucleus (LGN). From the LGN, visual information is carried by the other white matter tract, the optic radiation, to the V1.

Primary visual cortex (V1)

In primates, including humans, V1 is located in the posterior part of the cerebral cortex (occipital lobe) and is generally considered as the earliest cortical visual region. V1 is approximately equivalent to anatomical defined location of the striate cortex or Broadmann's area 17 and characterized by a high-myelinated layer called "stria of Gennari" (Zilles, 1986; Roland et al., 1994).

A number of neuroanatomical and electrophysiological studies have investigated a role of the V1 in visual information. For example, it is known that the visual information from the left and right retina are integrated in V1 at first by combining the contra and ipsi-lateral input from LGN neurons (Solomon et al., 2007). It is also known that the V1 has selectivities for specific visual properties, such as color (Livingstone & Hubel, 1984), binocular disparity (Ohzawa et al., 1990), orientation (Hubel & Wiesel, 1962) and direction of motion (Hawken et al. 1988). In addition, neuropsychological studies in humans suggested that lesions in the V1 cause a loss of conscious visual experiences (Weiskrantz et al., 1974; Sanders et al., 1974). The V1 is also an important cortical area which transmits visual signals to higher-order visual areas in the dorsal and ventral occipital lobe, each of which are involved in spatial information processing and categorical information processing, respectively (Ungerleider & Mishkin, 1982; Felleman & Van Essen, 1991; Van Essen et al., 1992). Therefore, a series of neuroanatomical, electrophysiological, and neuropsychological studies have shown converging evidence on the importance of the V1 to understand the neurobiological basis of the human vision.

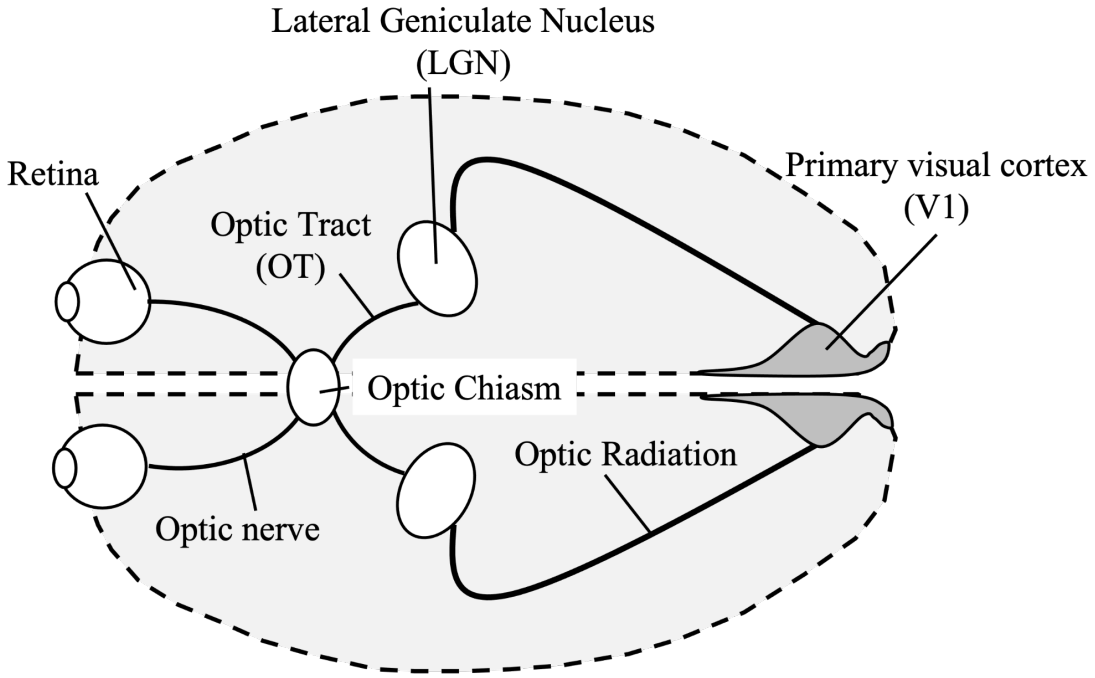

Figure 1.2. White matter tracts in the early part of the visual pathway. The visual information received at the retina transmitted via white matter tracts (optic nerve, and optic tract) to the LGN. Then, visual information processed in LGN is transmitted to V1 via white matter tract, optic radiation.

1.1.3 Individual differences in the human V1

While the V1 is one of the most widely studied regions in the cerebral cortex, there is one question which is not yet fully addressed: why the human V1 size has large individual differences. Previous post-mortem anatomical and neuroimaging studies have demonstrated that there are approximately three-fold range individual differences in size of V1 of both post-mortem and living human brains (Stensaas et al., 1974; Andrews et al., 1997; Amunts et al., 2000; Dougherty et al., 2003; Schwarzkopf et al., 2011; Benson et al., 2021) and these individual differences cannot be explained by the size of whole brains (Andrew et al., 1997; Benson et al., 2021). In addition, some studies reported a correlation between size of V1 and visual perception (Duncan & Boynton, 2003; Schwarzkopf et al., 2011; Song et al., 2013, 2015; Genç et al., 2015; Bergmann et al., 2016; Himmelberg et al., 2022). However, it is not clear what factor related to these individual differences in the size of V1.

One approach to improve understanding of individual differences in humans is to measure covariance across brain regions properties (Dougherty et al., 2003; Mechelli et al., 2005). Until recent progress of neuroimaging methods (see subchapter 1.2 “Neuroimaging method for living human brain”), structural properties of the visual pathways in humans were mostly studied in the post-mortem anatomical studies (Andrews et al., 1997; Zworykin, 1980; Johnson et al., 1987; Amunts et al., 2000). A previous post-mortem study (Andrews et al., 1997) reported a correlation between size of V1 and OT in post-mortem human brains. This result suggests that V1 size may covary with the property of fibers from RGCs because the OT is white matter tract composed of axons from RGCs. However, there is no proof that this finding can be generalizable to living human brains considering the fact that volumetric measurement of brain areas in the post-mortem brains can differ from that of living humans due to shrinkage of the post-mortem fixed brains. In addition, since post-mortem studies must be performed in a relatively smaller number of brains, it is also not clear how much findings can be generalizable to a large population. In the next subchapter, I will review the methodology of neuroimaging using magnetic resonance imaging (MRI), which enables us to address questions about individual differences of the visual system in the living human brains.

1.2 Neuroimaging method for living human brain

MRI is a method to acquire images of internal structure of biological tissues, including human brains, invented in the 1970’s (Lauterbur, 1973; Garroway et al., 1974; Kumar et al., 1975; Edelstein et al., 1980). Since its inception, the MRI method has substantially developed and becomes one of the most powerful methods to measure the structure and function of living human brains non-invasively. In this subchapter, I describe the MRI data acquisition and analysis methods used in my study: functional MRI (fMRI), diffusion MRI (dMRI) and tractography.

1.2.1 Functional MRI (fMRI)

Overview

FMRI enables measurement of the brain activity in living humans with relatively higher spatial resolution (1-3 mm isotropic). FMRI can be also used to investigate functional specialization of the human brain, by localizing areas related to specific types of visual stimulus such as motion (Huk et al, 2001), color (Engel et al., 1997), and object (Grill-Spector et al., 1998). In addition, this method can be also used to identify the position of the V1 using retinotopic mapping methods (see below) and quantify the size of the V1 in individual human subjects (Benson & Winawer, 2018).

Principle of fMRI

Hemoglobin without bind oxygen (deoxyhemoglobin) and hemoglobin with bind oxygen (oxyhemoglobin) show different magnetic properties; deoxyhemoglobin is paramagnetic and oxyhemoglobin is diamagnetic. When neurons are activated, an amount of oxygen in local capillaries decreases. Then oxyhemoglobin passes oxygen to the neurons, resulting in a temporary increase of deoxyhemoglobin in the capillaries. A few-seconds time-delayed increase in cerebral blood flow causes increases of oxyhemoglobin and decreases of deoxyhemoglobin. When the ratio of deoxyhemoglobin changes in the blood, we could identify such change using MRI, as the blood oxygen level dependent (BOLD) signals in animal brain (Ogawa & Lee, 1990; Ogawa, Lee, Kay, & Tank, 1990; Ogawa, Lee, Nayak, & Glynn, 1990) and human brain (Kwong et al., 1992; Ogawa et al., 1992; Bandettini et al., 1992). Currently, fMRI, which is a MRI method to localize brain activity based on BOLD signal, is considered as the best non-invasive method to measure human brain activity in terms of spatial resolution (Huettel et al., 2014).

Identify visual field maps from fMRI retinotopy data

One of the most successful applications of the fMRI is a measurement of retinotopic maps in living human brains. The retinotopy is an organized map of the visual field in brain areas, in which a spatial layout of visual input in the retina is maintained as a topological representation of the visual field in visual areas, such as V1 (Figure 1.3). A study of retinotopy has a long history, since classical lesion studies on the human brain discovered the association between location of cortical lesion and visual field loss, suggesting that the spatial arrangement of the image is maintained in the occipital cortex (Henschen et al., 1893; Inouye, 1909; Holmes, 1918). In later 1990's, several groups demonstrated that one can measure retinotopic maps of human brains by performing fMRI measurements when human subjects observe visual stimuli appeared in variable location (DeYoe et al., 1996; Engelet al., 1997; Sereno et al., 1995). These methods have become more sophisticated by development of computational, model-based methods explaining how populations of cells in each voxel represent the visual field (Dumoulin & Wandell, 2008) and methods to combine fMRI and structural MRI to improve an accuracy of retinotopic mapping (Benson & Winewer, 2018). To date, retinotopic mapping method using fMRI is widely used to identify locations of the V1 and other visual areas, as well as evaluating their properties in relation to disease (Wandell & Winawer, 2011).

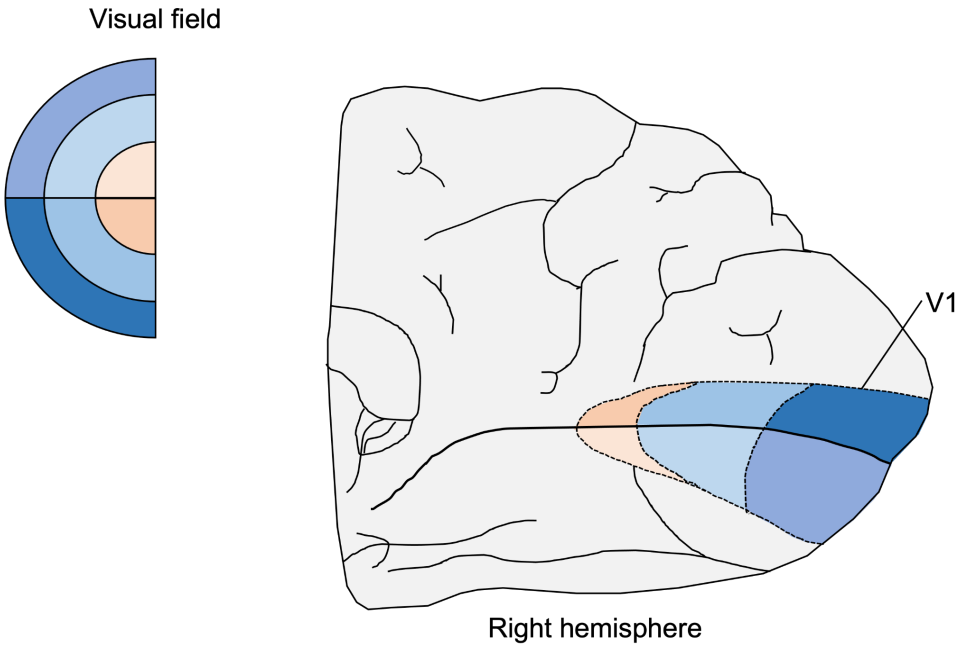

Figure 1.3. Schematic illustration of the retinotopic map in human V1. The visual information projected to the left visual field is transmitted to the right V1 (dotted line). Visual inputs in the upper half of the visual field and lower half of the visual field are projected to the dorsal and ventral part of V1, respectively. Color indicates visual field represented in different parts of V1.

1.2.2 Diffusion MRI (dMRI)

Overview

DMRI is a method to measure diffusion of water molecules using the MRI. Since diffusion of water molecules are restricted by biological tissue, this method can be also used to measure orientation of biological structure, including nerve fibers in human white matter (Rokem et al., 2017). Currently, in neuroscience, dMRI is used to measure both macroscopic (tract size) and microstructural measurements (biological tissue properties) of white matter tracts (Thiebaut de Schotten et al., 2011; Amemiya et al., 2021). In a common practice, modern neuroimaging studies evaluate these measurements on human white matter in relation to disease (Ogawa et al., 2014; Duan et al., 2015), development (Lebel et al., 2012), and learning (Yeatman et al., 2014).

Principle of dMRI

DMRI measures the direction of water diffusion in each data point (voxel) of the brain. It is known that water molecules move randomly (Brownian motion). However, in biological tissues, diffusion of water molecules are restricted by tissue microstructure, such as membranes. In particular, water molecules in white matter tracts diffuse in anisotropic direction because water diffusion is restricted to direction along the white matter tract (Huettel et al., 2014). This contrasts with properties of diffusion in other parts of the brain, such as cerebrospinal fluid (CSF), where water molecules diffuse isotropically because of no tissue structure restricting water molecule movement.

In dMRI, we measure magnitude and orientation of diffusion of water molecules using MRI. To perform dMRI measurements, a pair of magnetic field gradient pulses, motion probing gradient (MPG), must be applied. The first pulse disperses the spin phases of water molecules. The second pulse, same magnitude but opposite direction of the first pulse, realigns the phases and refocuses the signals (Figure 1.4). If water molecules diffusion along the orientation of MPG in between two pulses, the second pulse cannot refocus the phases perfectly, which leads to signal loss. By applying a pair of MPG, we can measure the magnitude of diffusion as a loss of the MR signal (Mori & Zhang, 2006). By repeating this measurement by changing the direction of the MPG, one can measure the magnitude of diffusion in each direction. In a subsequent analysis of dMRI, this information will be used to estimate diffusion orientation in each voxel.

While there are several key parameters for the dMRI acquisition, b-value is one of essential parameters which affect properties of diffusion contrast (Le Bihan et al., 1986). The b-value is defined as follows:

$$\text{b-value} = \gamma^2 G^2 t^2 (\Delta - \frac{t}{3}) \qquad (1.1)$$

while γ is gyromagnetic ratio, G is magnitude of MPG, t is a duration of MPG, and Δ is time between MPGs. It is generally known that there is a trade-off between contrast and signal-to-noise ratio in dMRI, such that measurements at higher b-values can get higher contrast but have lower signal-to-noise ratio (Raffelt et al., 2012). In addition, recent studies also provide evidence that different b-values have sensitivities for different types of water molecule movements, such as intracellular diffusion and extracellular diffusion (Assaf & Basser, 2005). Therefore, dMRI data acquired using multiple b-values can be also used to estimate microstructural properties of white matter in each voxel, as described in later subchapter (Zhang et al., 2012).

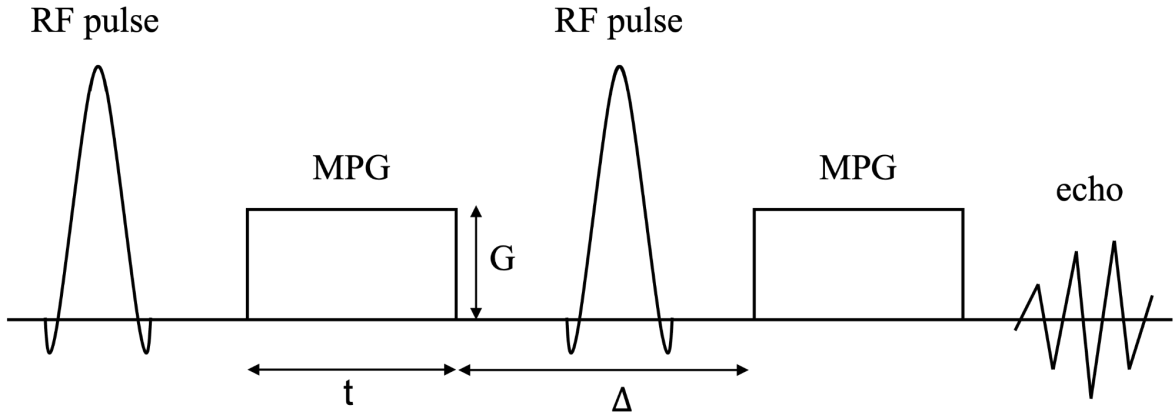

Figure 1.4. DMRI data acquisition sequence. Schematic illustration of dMRI pulse sequence design. DMRI sequence consists of a pair of the radio frequency (RF) pulses and a pair of the motion probing gradient (MPG). Echo is observed after each sequence. The b-value is calculated on the basis of G (magnitude of the MPG), t (duration of the MPG), Δ (time between MPGs), which are shown in the figure. Details are written in subchapter “diffusion MRI (dMRI)”.

Diffusion Tensor Model

DMRI measurements offer a magnitude of water diffusion in individual voxels along a specific number of directions, which correspond to a number of the MPG used during measurements. However, at this stage, the data is too sparse to infer three-dimensional fiber orientation in each voxel, since actual measurements are performed in a limited number of directions. Therefore, in a standard practice, researchers fit a model about orientation distribution of diffusion signals to the dMRI data, in order to estimate three-dimensional fiber orientation from dMRI measurements.

The most simplest form of the model is the diffusion tensor model (DTM), which uses a tensor model to represent the water diffusion as a three-dimensional ellipsoid defined by three eigenvectors (Basser et al., 1994a, 1994b). The largest diffusion direction in DTM is called the principal diffusion direction (PDD), which can be used as a proxy for fiber orientation in each voxel. In addition, DTM provides statistics of diffusion signals in each voxel such as fractional anisotropy (FA), which is an estimate of the degree of anisotropic diffusion. FA is defined as follows:

$$FA = \sqrt{\frac{1}{2}} * \sqrt{\frac{(\lambda_1-\lambda_2)^2+(\lambda_2-\lambda_3)^2+(\lambda_3-\lambda_1)^2}{\sqrt{\lambda_1^2+\lambda_2^2+\lambda_3^2}}} \quad (1.2)$$

while $\lambda_1, \lambda_2, \lambda_3$ are eigenvectors of DTM. When FA values closer to 1 mean water diffusion is more anisotropic and closer to 0 means more isotropic (Figure 1.5). Since FA is known to be sensitive to many different types of white matter tissue changes (Wandell, 2016; Assaf et al., 2019) and highly reproducible measurements (Kruper et al., 2021), FA is widely used in neuroscience studies as a metric to quantify properties of the white matter properties.

Despite its advantages, the DTM has several limitations as a model to describe white matter tissue properties. One notable limitation is that the DTM is known to be too simplistic to describe specific types of white matter microstructural properties. As shown in Figure 1.5, there are many factors which can affect FA; for example, both lower axon density and lower myelin density can lead to lower FA, because both can increase anisotropy of water diffusion. For this reason, there is an ongoing effort to establish a more complex model to explain diffusion signals for identifying more biologically specific metrics.

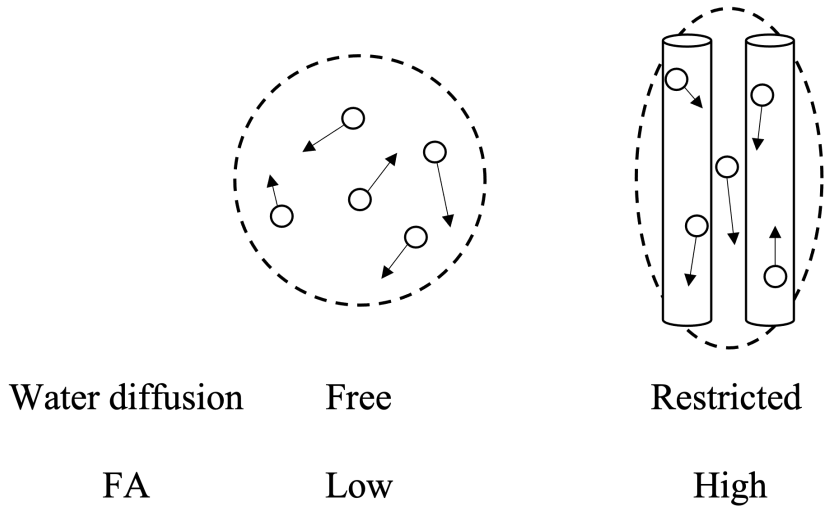

Figure 1.5. Anisotropy of diffusion signal in white matter and underlying tissue structure. A schematic illustration of fractional anisotropy (FA), which is a degree of anisotropic diffusion. In general, FA becomes higher when water diffusion water diffusion is more restricted by white matter microstructure. FA value is affected by several different types of microstructural properties such as the degree of the fiber density and dispersion, myelination.

Neurite orientation dispersion and density imaging (NODDI)

Neurite orientation dispersion and density imaging (NODDI), is one of advanced diffusion models aiming to overcome aforementioned limitations of the DTM (Zhang et al., 2012).

NODDI is a multi-compartment model to characterize the tissue microstructure within the voxel by using three parameters: intracellular compartment, extracellular compartment, and free water. The key assumption of this model is that these compartments have different degrees of restriction and different speed of water diffusion. For example, NODDI assumes that waters within axons are most restricted and diffuse at the slowest speed. NODDI also assumes that there are water molecules outside axons but within white matter tracts; diffusion of those molecules are still restricted by white matter microstructure, but an amount of restriction must be much less and diffusion speed must be faster compared with those of intracellular water molecules. The intra-neurite compartment is modeled by a collection of thin sticks, aiming to represent neural axons. The extra-neurite compartment is modeled by a diffusion tensor, aiming to represent relatively less restricted water molecule diffusion outside cells but still inside white matter tracts. The free water compartment is modeled by isotropic diffusion. The NODDI aims to explain diffusion signal (A) by combination of these compartments as follows:

$$A = (1 - v_{fw})(v_i A_i + (1 - v_i)A_e) + v_{fw}A_{fw} \qquad (1.3)$$

while v_i and v_{fw} are the volume fractions of the intra-neurite and free water compartments in each voxel, and A_i , A_e and A_{fw} are the normalized signal of the intra-neurite, extra-neurite, and free water compartments in each voxel, respectively. Using parameters estimated in this formula, NODDI estimates several parameters about microstructural properties, such as intracellular volume fraction (ICVF) and orientation

dispersion index (ODI), each of which are hypothesized to be correlated with neurite density and orientation dispersion measured by histology, respectively (Figure 1.6; Molink et al., 2017; Schilling et al., 2018).

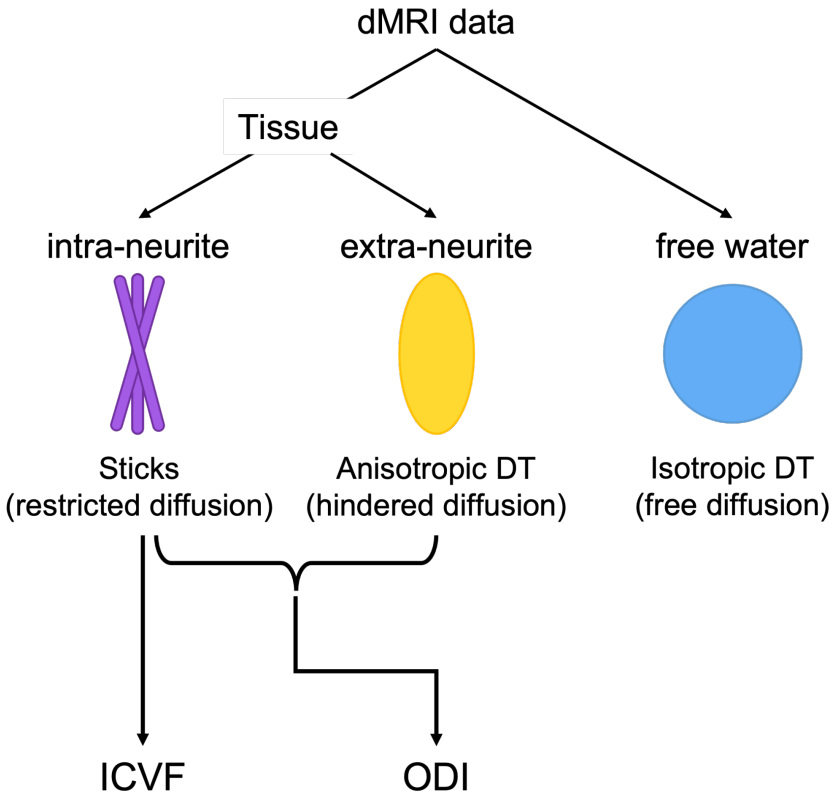

Figure 1.6. Schematic figure of the NODDI model and parameters. NODDI aims to explain diffusion signals in each voxel based on three tissue compartments. The intra-neurite compartment is modeled by a collection of thin sticks (restricted diffusion) and the extra-neurite compartment is modeled by an anisotropic diffusion tensor (DT) (hindered diffusion), while free water is modeled by an isotropic DT (free diffusion). ICVF and ODI are parameters representing microstructural properties calculated by intra-neurite compartment and both intra-neurite and extra-neurite compartments, respectively.

Tractography

In order to analyze properties of white matter tracts, one needs to estimate not only fiber orientation distribution in individual voxels, but also estimate how each voxel is connected to each other to understand a trajectory of white matter tracts. Tractography is a method to reconstruct estimated white matter tracts by tracking oriented water diffusion of each voxel in dMRI data. This requires an algorithm to track the orientation of diffusion signals in individual voxels and then move toward a different voxel. This process generates an estimate of three-dimensional trajectory, which is called streamlines. While single streamline is not a proxy of individual axons, the aim of tractography is to generate streamlines for identifying a trajectory of major white matter tracts in living humans.

There are many different types of tractography algorithms, which have developed during a history of dMRI studies (Wandell, 2016). The classical tractography, developed during the late 1990's, is deterministic tractography (Mori et al., 1999; Conturo et al., 1999) which generates streamline by always following the PDD of the DTM of the voxel (Figure 1.7A). Later, probabilistic tractography (Behrens et al., 2003; Behrens et al., 2007; Tournier et al., 2012) has been developed. This method generates streamlines by taking diffusion signals as a probability density function (Figure 1.7B). It follows directions with larger diffusion signals in higher probability, while it also follows directions with relatively lower diffusion signals in lower probability. Because this algorithm has higher sensitivity of white matter pathway with the curved path, such as the optic radiation, the probabilistic tractography is often used to study visual white matter pathways (Sherbondy et al., 2008).

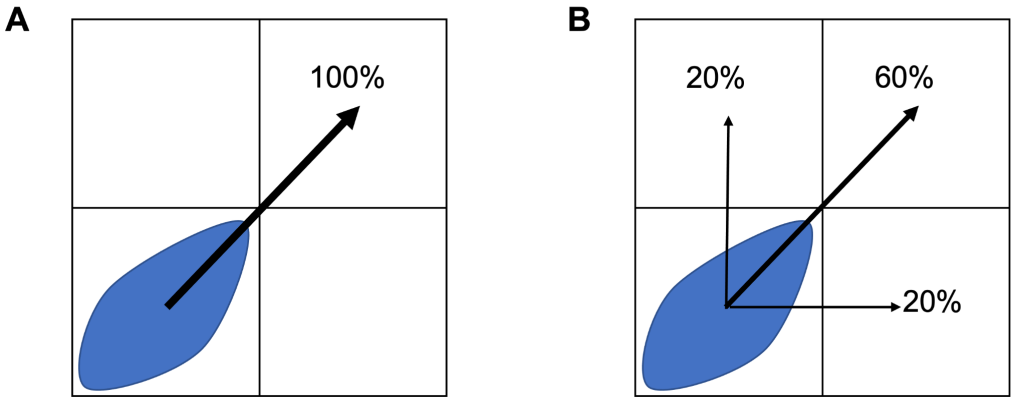

Figure 1.7. Schematic figure of the tractography. A. Deterministic tractography is an algorithm to track orientation of diffusion signals, by always tracking the most principal diffusion direction in the voxel. **B**. Probabilistic tractography regards the shape of the diffusion signal as a probability distribution function and determines the tracking direction probabilistically based on the distribution of diffusion signal in each voxel.

Tractometry

To analyze tissue properties along white matter tracts, one can combine a model of diffusion signal in individual voxels (DTM and NODDI) and tractography. For example, one can statistically evaluate metrics derived from DTM and NODDI (FA, ICVF, and ODI) along a specific white matter tract identified by tractography in individual subjects. This profile can be used to compare the data across subjects (Yeatman et al., 2012). This procedure for evaluating metrics along white matter tract using dMRI is called tractometry. Currently there are several software tools available to perform tractometry analysis on the dMRI data (Yeatman et al., 2012; Yendiki et al., 2011; Kruper et al., 2021). This method is now widely used to compare healthy and disease populations (Ogawa et al., 2014) and evaluate the age difference of white matter tract tissue properties (Lebel et al., 2011; Yeatman et al., 2014; Amemiya et al., 2021). In this dissertation, I use this method to evaluate individual differences of white matter tracts in the visual system, such as the OT.

1.3 Aim of the dissertation

In previous subchapters, I described the literature of past studies on the human visual system and a progress of MRI methods as a measurement of structure and function of the living human brains. However, even to date, it is still unclear what is the origin of a large individual difference of the V1 size in living humans despite past findings of structural covariance with OT. The other remaining question is how much inter-subject variability of brain areas in the human visual system, such as V1, is related to genetic factors.

The progress of the neuroimaging method, as highlighted in subchapter 1.2, makes it possible to measure both retinotopic map and white matter tracts in living humans by using fMRI and dMRI, respectively. In the next chapter, I describe a study which aimed to investigate the relationship between individual differences in V1 and OT in the living human brains by combining these two neuroimaging methods.

Chapter 2. Structural covariance and heritability between white matter tract and cortical area in the visual system of living human brains

2.1 Introduction

Human brains differ on many levels, including gene expression, morphology of macro-scale anatomical landmarks, tissue properties of cortical areas and white matter tracts, size of cortical areas, and perceptual performance. One notable example at the cm scale is V1, which varies in size between human brains by up to a factor of 3-4 (Stensaas et al., 1974; Andrews et al., 1997; Amunts et al., 2000; Dougherty et al., 2003; Schwarzkopf et al., 2011; Benson et al., 2021). These individual differences are not explained by variation in whole brain size (Andrews et al., 1997; Benson et al., 2020). Moreover, some studies have found that individual differences in V1 size can be related to properties of visual perception (Duncan & Boynton, 2003; Schwarzkopf et al., 2011; Song et al., 2013, 2015; Genç et al., 2015; Bergmann et al., 2016; Himmelberg et al., 2022). Understanding what factors influence individual differences in V1 size is likely to clarify our understanding of how human visual processing and perception vary across people.

One approach to improve understanding of individual differences is to measure covariance across brain regions (Dougherty et al., 2003; Mechelli et al., 2005). The logic is that if properties of two related structures covary, then these structures may mature by common mechanisms. Andrews and colleagues (1997) analyzed post-mortem human brains to investigate the relationship between V1 and the OT, a white matter tract composed of axons from RGCs. They found that V1 size was significantly correlated with OT size, suggesting that there are common factors determining individual variability in this fiber tract and V1. This study measured a relatively small number of post-mortem brains. Here I investigated similar questions in a much larger sample of living brains.

Recent progress in non-invasive neuroimaging methods have opened an avenue to quantify the structural properties of cortical areas and white matter tracts in living humans. Specifically, fMRI enables the identification of visual field maps including V1 (Wandell and Winawer, 2011), whereas diffusion MRI (dMRI) and tractography enable one to measure properties of white matter tracts including the OT (Rokem et al., 2017). dMRI provides both macroscopic (tract volume) and microstructural measurements (such as fractional anisotropy, FA), each of which provide complementary information about anatomical variability of white matter (Thiebaut de Schotten et al., 2011; Amemiya et al., 2021). By taking advantages of these two methods, it is possible to build a large neuroimaging dataset including both fMRI and dMRI data, thus enabling comparisons between them in a large sample (Van Essen et al., 2012). One such dataset is the Human Connectome Project (HCP) 7 Tesla Retinotopy dataset, which includes fMRI data on retinotopic mapping acquired at 7T and structural and diffusion MRI data acquired at 3T in 178 healthy young adults (Benson et al., 2018). In addition, this dataset includes data

acquired from monozygotic (MZ) and dizygotic (DZ) twin pairs, enabling the assessment of heritability. Heritability is complementary to variability: heritability measures the contribution of genetics to individual differences, and hence addresses the question of where variability in neuroimaging measures arise (Benson et al., 2021).

In this study, I analyzed the HCP 7T Retinotopy dataset to investigate the structural covariance of V1 and OT in living humans to understand how much individual variability in human V1 size is related to properties of the OT. I identified V1 by combining fMRI with structural MRI data (Benson & Winawer, 2018) and the OT by analyzing dMRI data (Sherbondy et al., 2008). I then evaluated structural covariance between V1 size and macrostructural and microstructural measures of OT properties. Finally, I examined the heritability of each structure by analyzing twin data. This study has implications for the biological origin of individual differences in human V1 size, a key cortical area for distributing visual information to the rest of the brain.

2.2 Materials and Methods

2.2.1 Subjects

I analyzed data from 178 subjects (aged 22-35; 107 females, 71 males) whose structural MRI and dMRI data, as well as their retinotopic mapping fMRI data, were collected as part of the Young Adult HCP (Van Essen et al., 2013). Population receptive field models from the retinotopic mapping experiment were solved and published as a separate dataset (Van Essen et al., 2013; Benson et al., 2018). This dataset includes 53 MZ pairs and 31 DZ pairs. All subjects in the HCP dataset provided written informed consent. Further details of the dataset are described in previous publications (Van Essen et al., 2013; Benson et al., 2018).

2.2.2 MRI data acquisition and preprocessing methods

Structural MRI data acquisition and preprocessing

T1-weighted (T1w) structural MR images with an isotropic voxel size of 0.7 mm were acquired from a 3T MRI scanner and used for surface-based analysis of fMRI data as well as for identifying V1 in individual subjects. The dataset was preprocessed by the HCP consortium. This preprocessing included automated tissue segmentation implemented in FreeSurfer (Fischl, 2012) and reconstructing the white and pial cortical surfaces (Glasser et al., 2013).

Diffusion MRI data acquisition and preprocessing

I analyzed the dMRI dataset acquired by the HCP consortium. In brief, whole-brain dMRI data were corrected at an isotropic voxel size of 1.25 mm using 3T MRI. The dMRI data was preprocessed by the HCP consortium to correct eddy-current artifacts and susceptibility-induced image distortions (Andersson et al., 2003; Glasser et al., 2013;

Andersson & Sotiropoulos, 2016). The dMRI data consists of three types of diffusion-weighted images (b = 1000, 2000, 3000 s/mm^2) as well as non-diffusion weighted images (b = 0 s/mm^2).

Tensor-based analysis. I divided the dMRI data into three datasets acquired with different b-values. I used b = 2000 s/mm^2 as the test dataset. This choice of b-value reflects a tradeoff between signal-to-noise ratio (SNR) and specificity: dMRI data acquired with lower b-value has higher SNR but weaker image contrast and less specific to the intracellular diffusion signal (Raffelt et al., 2012). The data acquired with other b-values were used as validation datasets to assess generalizability. I fit a tensor model to each voxel in the dMRI data using a least-squares algorithm implemented in mrDiffusion of vistasoft software (https://github.com/vistalab/vistasoft/). The tensor fits were then used to derive fractional anisotropy (FA; Basser & Pierpaoli, 1996).

NODDI analysis. I used neurite density and orientation dispersion imaging (NODDI; Zhang et al., 2012) to evaluate tissue properties of the OT. NODDI is a model assuming multiple types of microstructural environment and aims to provide biologically meaningful parameters from dMRI signals. I fit NODDI to the whole dMRI dataset including all b-values using the NODDI MATLAB toolbox (http://mig.cs.ucl.ac.uk/index.php?n=Tutorial.NODDImatlab). From these fits, I obtained intra-cellular volume fractions (ICVF) and orientation dispersion index (ODI).

FMRI Image acquisition and preprocessing

I used the fMRI data already preprocessed by the HCP Consortium with the HCP pipelines (Glasser et al., 2013; Vu et al., 2017; Benson et al., 2018). In brief, whole-brain fMRI data were collected at an isotropic voxel size of 1.6 mm using 7T MRI. During the fMRI data acquisition, subjects were instructed to perform a fixation task that required them to maintain gaze at the center of the screen; simultaneously, they were presented with retinotopic mapping stimuli. These stimuli were constructed from slowly moving apertures that contained dynamic colorful textures (Dumoulin & Wandell, 2008; Benson et al., 2018).

2.2.3 MRI data analysis methods

Diffusion MRI data analysis

Defining ROIs for tractography. I identified regions of interest (ROIs) for tractography based on T1w images in each individual subject. The optic chiasm was defined based on Freesurfer's automated segmentation (Fischl, 2012). I then defined the LGN ROIs manually by following streamlines found using deterministic tractography from a seed-region in the optic chiasm to their termination points. The LGN ROI is defined as a 4 mm radius sphere covering these endpoints (Takemura et al., 2019). I also identified the V1 ROI for tractography using the Brodmann Area atlas implemented in Freesurfer. I used this atlas, rather than V1 boundaries identified using fMRI data because, for the purpose of tractography, the larger Brodmann V1 ROI may improve the sensitivity of tractography

for the purposes of identifying the optic radiation (OR). The V1 ROIs were redefined using functional data for the purpose of quantifying V1 size (see below; Functional MRI data analysis).

Tractography. I performed tractography on the dMRI data (with b = 2000 s/mm^2) to identify the OT using ConTrack (Sherbondy et al., 2008). ConTrack is a probabilistic tractography method specifically designed for identifying visual white matter tracts by selecting the most probable path of the white matter tract connecting two ROIs. Specifically, I sampled 5,000 candidate streamlines connecting the optic chiasm and the LGN ROIs in both hemispheres (angle threshold, 90°; step size, 1 mm; maximum streamline length, 80 mm). I then refined OT streamlines using the following criteria. First, I selected 100 streamlines with the highest scores in the ConTrack scoring process (Sherbondy et al., 2008). Second, I removed outlier streamlines with (1) length > 3 S.D. longer than the median streamline length in the tract, or (2) position > 3 S.D. away from the median position of the tract using AFQ MATLAB toolbox (Yeatman et al., 2012).

In addition to the OT, I also identified the OR. For the OR, I used ConTrack to generate streamlines connecting the LGN and V1 ROIs and to reject outlier streamlines (Takemura et al., 2019).

Estimating the cross-section area of the OT. I quantified the cross-section area of the OT to match the dependent measures from previous anatomical work (Andrews et al., 1997). To do this, I first identified voxels that intersected the OT streamlines in each coronal section of the dMRI data. I then multiplied the voxel size in the section (1.25 x 1.25 mm^2) by the voxel count to calculate the cross-section area in each coronal section. Finally, I averaged the cross-section area across coronal sections to obtain the mean cross-section area of the OT in each individual subject. When averaging, I excluded the 10% of sections nearest the optic chiasm ROI and the 10% of sections nearest the LGN ROI. This reduces the possibility of including the optic chiasm or the LGN in my estimate of OT cross-section area. For comparisons with V1 data, I averaged the data from the left and right hemisphere of each individual subject.

Estimating the cross-section area of the OT adjusted for angle between the coronal section and OT. In addition, I also estimated OT cross-section area adjusted for the angle between the coronal section and OT based on the geometry of tilted cylinder (Kapitány et al., 2013):

$$\text{Adjusted OT cross-section area} = \cos\alpha \times \text{OT cross-section area} \qquad (2.1)$$

where α is an angle between the coronal section and OT.

Evaluating tissue properties of the OT. I evaluated tissue properties of the OT using the AFQ MATLAB toolbox (Yeatman et al., 2012; Duan et al., 2015; Takemura et al., 2019). Briefly, I resampled each streamline to 100 equidistant nodes. Tissue properties (FA, ICVF, and ODI) were calculated at each node of each streamline. The properties at each node were summarized by taking a weighted average of the tissue measurements of

each streamline within that node. The weight of each streamline was based on the Mahalanobis distance from the tract core to minimize partial voluming effects with tissue or cerebrospinal fluid outside the OT. I excluded the first and last 10 nodes from the calculation of the tissue property of the tract core to further reduce any partial voluming effects with neighboring structures, which often occur near the endpoints of the tract. I averaged data from the remaining 80 nodes to obtain a single-number summary of each tissue property (FA, ICVF, and ODI) for each subject. In the main analysis, the data from the left and right hemisphere were averaged to reduce noise for comparisons with V1. I performed the same analysis for the OR.

Functional MRI data analysis

Bayesian retinotopy analysis for identifying the V1 surface area. I measured the surface area of V1 in each subject by analyzing fMRI and structural MRI data. To do so, I first performed Bayesian analysis of retinotopic maps (Benson & Winawer, 2018), which combines traditional fMRI-based retinotopic mapping (Dumoulin & Wandell, 2008) with a retinotopic template (Benson et al., 2012, 2014). Specifically, this method identifies the retinotopic parameters of each surface vertex in visual cortex, as well as the boundaries between maps, using Bayesian inference in which structural MRI acts as a prior constraint and fMRI data as an observation. This analysis procedure has been demonstrated to reliably identify properties of the early retinotopic areas (V1/V2/V3) and is implemented in the publicly available neuropythy library (https://github.com/noahbenson/neuropythy).

The V1 ROIs were projected onto the mid-gray cortical surface mesh for measuring surface area. Surface area for each subject's V1 was calculated by summing the area of the mesh triangles and partial sub-triangles they contained. In the main analysis, I averaged the surface areas of V1 across hemispheres to reduce noise for a comparison with the OT data.

2.2.4 Experimental design and statistical analyses

Statistical evaluation

Correlation between the OT and V1. I quantified the correlation between the OT measurements (cross-section area, FA, ICVF and ODI) and V1 surface area by calculating the Pearson correlation coefficient between them. I report the P-value of the Pearson correlation and define the statistical significance as $P = 0.0125$, which is equivalent to $P = 0.05$ after Bonferroni correction for four comparisons. I note that this threshold might be too stringent for considering a correlation between FA and ODI (Zhang et al., 2012). While the main analysis was performed on the OT and V1 data averaged across hemispheres, I also separately analyzed the left and right hemisphere.

Correlation between OT measurements and signal-to-noise ratio of MRI images. I performed a supplementary analysis to evaluate how much the OT measurements (cross-section area, FA, ICVF, and ODI) correlate with the SNR of MRI images. An

accurate estimation of SNR for diffusion-weighted images is difficult because in these images, a loss of image signal intensity is associated with more diffusion, and the signal depends on the orientation of the motion probing gradient. Instead, I estimated the SNR of b = 0 images within the OT using the following equation comparing two b = 0 images (Reeder et al., 2005; Kida et al., 2016):

$$\text{SNR} = \sqrt{2} \times SI\,(first\ image) \,/\, SD\,(subtracted\ image) \qquad (2.2)$$

where SI (first image) is the mean signal intensity of the first b = 0 image within the OT. SD (subtracted image) is the standard deviation of signal intensity difference between first and second b = 0 images within the OT. I estimated the SNR of b = 0 image using this method by pooling the OT voxels in left and right hemispheres and calculated the Pearson correlation between SNR and OT measurements (cross-section area, FA, ICVF, and ODI) across subjects.

Evaluating inter-hemispheric correlation. I also tested the inter-hemispheric correlation of the OT measurements for evaluating the reliability of the measurement. To this end, I calculated the Pearson coefficient across hemispheres. I test interhemispheric correlations as a proxy for test-retest reliability on the assumption that the true values (without measurement noise) are highly correlated between hemispheres.

Evaluating test-retest reliability. I also analyzed the retest dMRI dataset acquired from 19 subjects who also participated in the retest scan. I then evaluated the test-retest reliability of OT measurements (cross-section area and FA) by calculating the intraclass correlation coefficient (ICC; Shrout & Fleiss, 1979) between the test and retest dataset.

Evaluating the influence of the inclusion of twin pairs on the correlation. I evaluated how much the inclusion of twin pairs, which may not be fully independent samples, affects the correlation between OT and V1. To perform this analysis, I generated a subsample of subjects in which I removed one member of each twin pair from the whole dataset and reassessed the OT-V1 correlation, leaving 94 subjects. Because either of the members of each twin pair could be removed, there are many to select the subset of subjects. Hence I generated subsamples of 94 subjects 10,000 times, and each time calculated the OT-V1 correlation to obtain a distribution of the correlation coefficient after the removal of twin pairs. This distribution was compared with the null distribution of the correlation coefficient, which was obtained by randomly choosing 94 subjects 10,000 times (without regard to twin status) and shuffling the association between OT and V1 data (see Figure 2.6C).

Evaluating heritability

I evaluated the heritability—i.e., the fraction of the variance for a given trait that is attributable to genetics—of the OT FA and of the surface area of V1 by comparing the correlations of these measurements between MZ twin pairs to the correlations between DZ twin pairs. I used the ICC when examining twin pairs. I then employed Falconer's formula (Falconer & Mackay, 1996) to estimate OT FA and V1 surface area heritability.

Falconer's formula is: $h^2 = 2(r_{MZ} - r_{DZ})$ (2.3)

where h^2 is the heritability index and r_{MZ} and r_{DZ} are the ICCs between MZ pairs and DZ pairs, respectively.

2.2.5 Code Accessibility

Code for reproducing figures and statistical analyses of this work is publicly available at a public repository (https://osf.io/t2kh3/). Codes were written in MATLAB 2015a and tested on Ubuntu 14.04 LTS. However, I cannot release data for reproducing the twin analyses because the family structure data belongs to the HCP's restricted dataset and thus cannot be shared without consent of the HCP Consortium. To reproduce analysis requiring family structure, researchers must apply for access to "Restricted Data" on ConnectomeDB (see https://www.humanconnectome.org/study/hcp-young-adult/document/wu-minn-hcp-consortium-restricted-data-use-terms).

2.3 Results

I identified V1 and the OT by analyzing functional, structural, and diffusion MRI datasets in the HCP Young Adult and the HCP 7T Retinotopy datasets (Figure 2.1A and 2.1B), in 178 subjects. Similar to previous works (Stensaas et al., 1974; Andrews et al., 1997; Amunts et al., 2000; Dougherty et al., 2003; Schwarzkopf et al., 2011), and as reported recently for this dataset (Benson et al., 2020), there is a considerable degree of inter-individual difference in V1 surface area, spanning a two-fold range (Figure 2.1C). Cross-section area and FA of the OT also exhibited considerable inter-individual differences (Figure 2.1D and 2.1E). In subsequent analyses, I focused on the relationship between individual differences of V1 and the OT in the HCP 7T Retinotopy dataset.

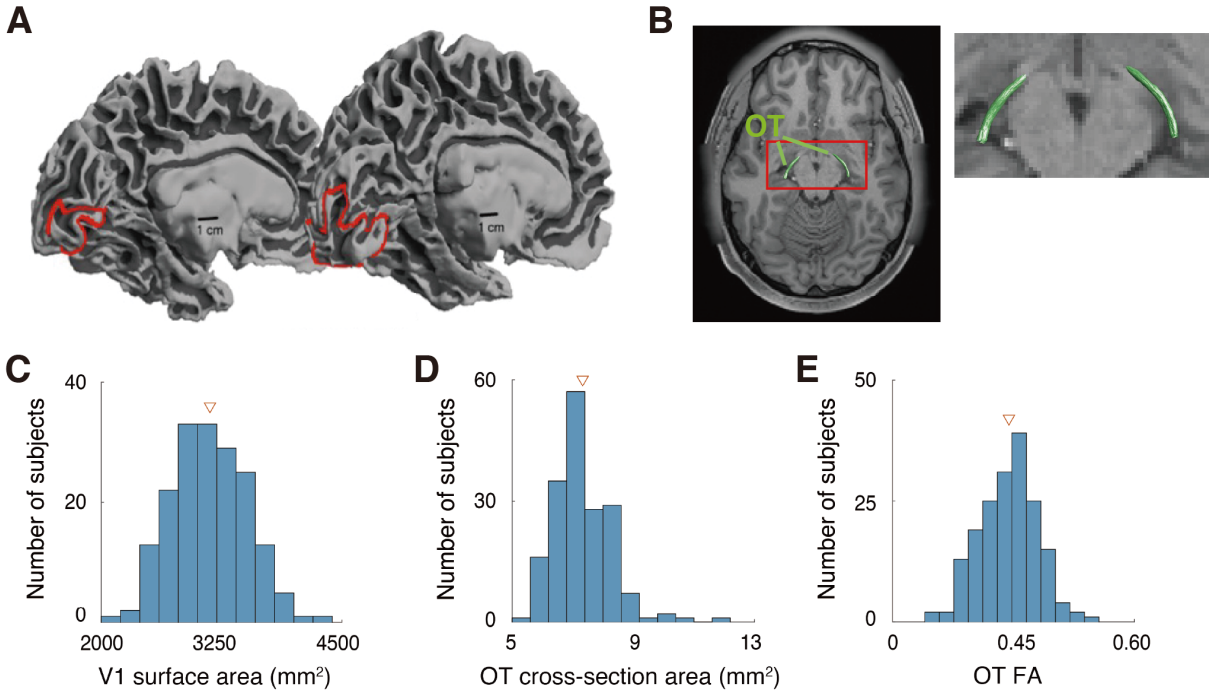

Figure 2.1. Individual variability of structural properties of the early visual system in human brains. **A.** Human V1 identified by fMRI-based retinotopy measurements. The locations of V1 in the left hemisphere of two subjects are shown as red lines on the mid-gray surface. The V1 surface area of these two hemispheres differs by a factor of 3.5 (left, subject 958976, 620 mm^2; right, subject 100610, 2180 mm^2). This image is adapted from Benson et al. (2020). **B.** Human optic tract (OT) of a representative subject (subject 100610), identified by dMRI-based tractography, overlaid on an axial slice of the subject's T1-weighted image. The red rectangle on the left panel indicates the region that is magnified on the right. **C-E.** Histograms of the V1 surface area (**C**), OT cross-section area (**D**), and OT FA (**E**) of individual subjects (N = 178) averaged across the left and right hemispheres. Triangles in each plot depict mean across subjects.

2.3.1 Correlation between V1 surface area and OT cross-section area

I first examined the correlation between V1 surface area and OT cross-section area, because such a correlation was reported in post-mortem anatomical work (Andrews et al., 1997). Figure 2.2A depicts a scatter plot comparing the V1 surface area and the OT

cross-section area. I did not find a statistically significant correlation between these measurements (r = -0.05; P = 0.5). I also did not find evidence of correlation when I separately analyzed the data from left and right hemispheres (r = 0.09 and 0.01 for left and right hemispheres, respectively) and treating data of each hemisphere as independent samples (r = -0.02; as done in Andrews et al., 1997). Therefore, I failed to replicate the previous anatomical finding in an *in vivo* neuroimaging dataset. The correlation coefficient remained almost the same even after adjusting the OT cross-section area for the angle between the coronal section and the OT (Figure 2.2B; r = -0.05).

This result differs from Andrews et al. (1997)'s post-mortem findings. It is unlikely that this mismatch occurs simply by chance, because when I randomly subsampled the HCP data into 29 samples (as used in Andrews et al., 1997), the probability of obtaining a correlation coefficient at least as high as Andrew et al. (1997; r = 0.48) is very low (Figure 2.3A; P = 0.0006). The correlation obtained in this study (r = -0.06) is also outside of the 95% confidence interval of the correlation coefficient in Andrews et al. (1997) estimated by bootstrapping their data (Figure 2.3B; r = 0.19 - 0.68).

One possible interpretation of this mismatch is that there is a high degree of measurement noise in my OT cross-section area estimates due to low spatial resolution. The voxel size of the dMRI dataset in the 3T HCP Young Adult dataset is 1.25 mm, isotropic. The cross-section area of the OT ranges from 5.1 mm^2 to 11.3 mm^2, according to Andrews et al. (1997). If I aim to estimate the volume of such a small tract with 1.25 mm voxel size, a large proportion of the OT voxels will be located on the border between the OT and neighboring tissue, and thus the estimates of OT size will depend on the placement of voxels (Figure 2.4). This will cause additional noise in the measurements and will mask true inter-individual differences in OT size. In contrast, measurements of diffusivity properties, such as FA, are likely to be less prone to this issue because one can calculate a weighted summary of tract FA by minimizing the weight of voxels located far from the tract core (Yeatman et al., 2012).

One metric of reliability is inter-hemispheric correlations. I computed this for the OT cross-section area and FA. A key assumption in this analysis is that measurements of the left and right OT in the same subject should be similar. While this assumption is only likely to be approximately correct, it provides a reasonable estimate of reliability because inter-hemispheric correlation was very high in a previous post-mortem study (r = 0.84, in data presented in Andrews et al., 1997). I found that the correlation between left and right OT cross-section areas was much smaller (Figure 2.5A; r = 0.38) than that between left and right OT FA (Figure 2.5B; r = 0.77). This difference in correlation coefficient was statistically significant ($P < .001$). In addition, I also evaluated reliability of OT measurements by analyzing retest dMRI data acquired from a subset of subjects (n = 19) who also participated in the retest scan. I also found that test-retest reliability (ICC) of OT cross-section area was much smaller (Figure 2.5C; ICC = 0.60) than that of OT FA (Figure 2.5D; ICC = 0.89). These results suggest that the OT cross-section area measurements based on dMRI are noisier than the FA measurements. I note that I obtained a high correlation between the left and right V1 surface area (Figure 2.5E; r =

0.76). This result motivated me to investigate the correlation between V1 surface area and OT FA, because FA is a more robust measurement for characterizing individual differences in OT structural properties.

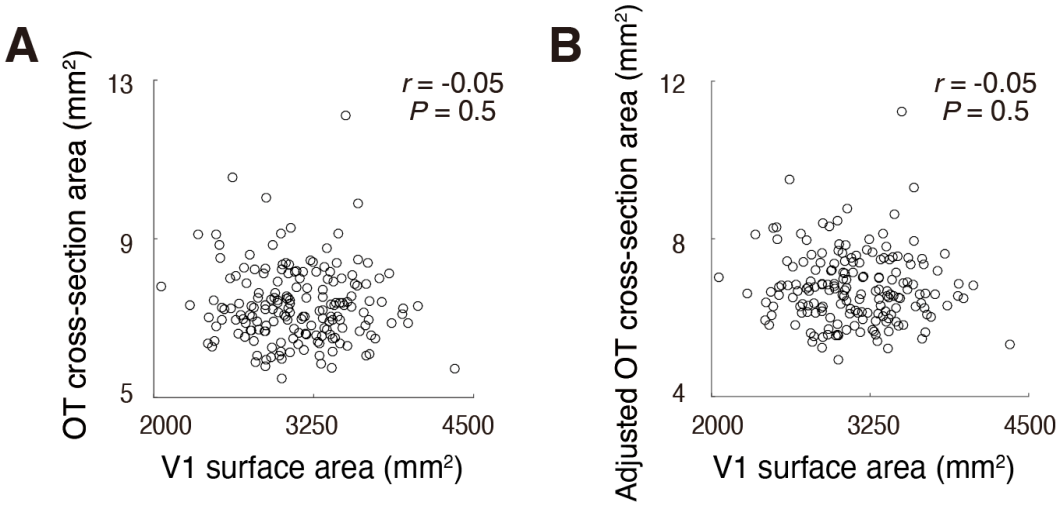

Figure 2.2. The correlation between V1 surface area and OT cross-section area. A. No significant correlation between V1 surface area (horizontal axis) and OT cross-section area (vertical axis). **B.** No significant correlation between V1 surface area and OT cross-section area adjusted for angle between the coronal section and OT.

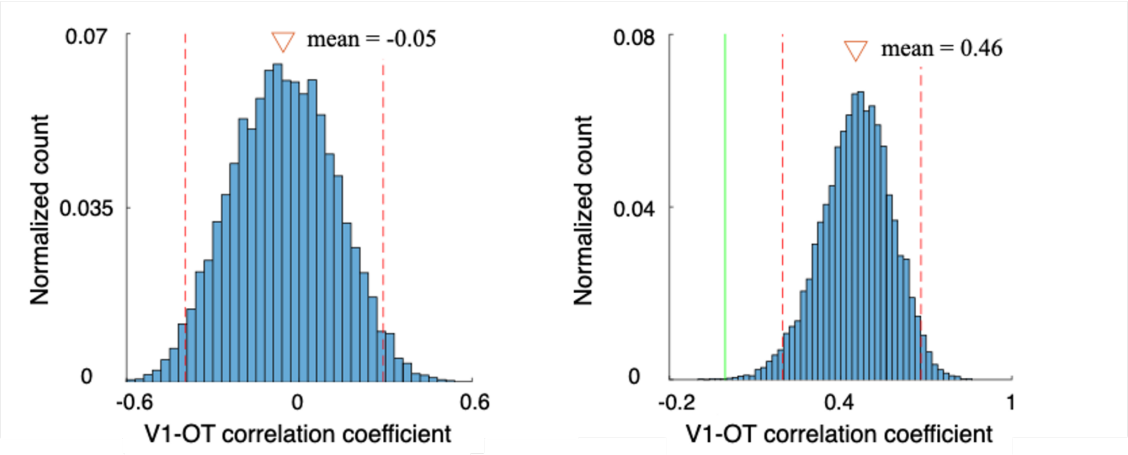

Figure 2.3. Difference in correlation between OT cross-section area and V1 surface area between studies is unlikely to be explained by random sampling alone. A. Distribution of correlation coefficients between OT cross-section area and V1 surface area when randomly subsampling the HCP data into 29 samples, which is equal to the sample used in Andrews et al. (1997). **B**. The histogram of correlation coefficient obtained by bootstrap analysis for correlation data presented in Andrews et al. (1997). The horizontal axis indicates correlation coefficients between V1 and OT size obtained in each bootstrap sample (from 10,000 bootstrap sampling). The vertical axis is a number (normalized count) of bootstrap samples. The mean correlation coefficient obtained from bootstrapping is r = 0.46, which is almost equivalent to the data presented in Andrews et al. (1997). The vertical red dotted line indicates top 5% and bottom 5% percentile from bootstrap sample, which corresponds to 95% confidence interval. The vertical solid green line indicates a correlation coefficient obtained in this study (r = -0.05).

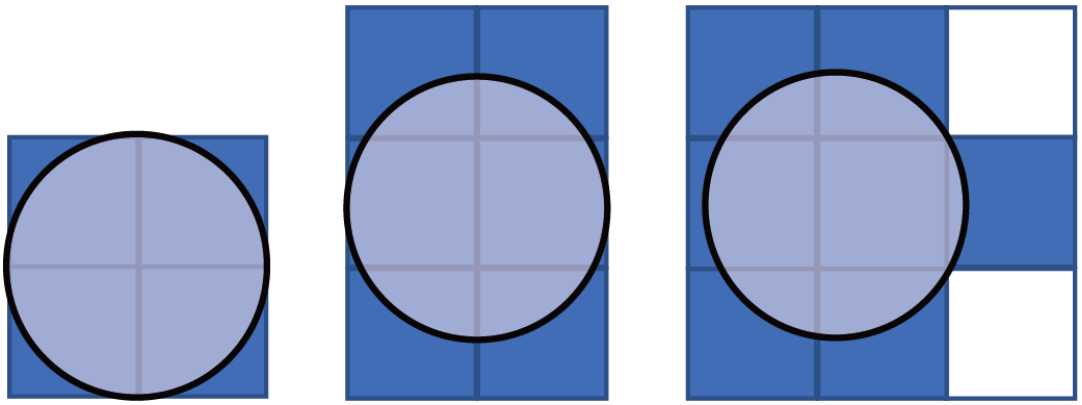

Figure 2.4. Schematic figure of the OT cross-section area estimation on dMRI data. Figure explaining how the spatial arrangement of voxels impacts the estimate of OT cross-section area when the spatial resolution of the measurements is limited. In all panels, the true cross-section area of the OT (light blue circle) is identical. However, the voxel count (dark blue) significantly differs across these three cases due to differences in the placement of the voxels (squares).

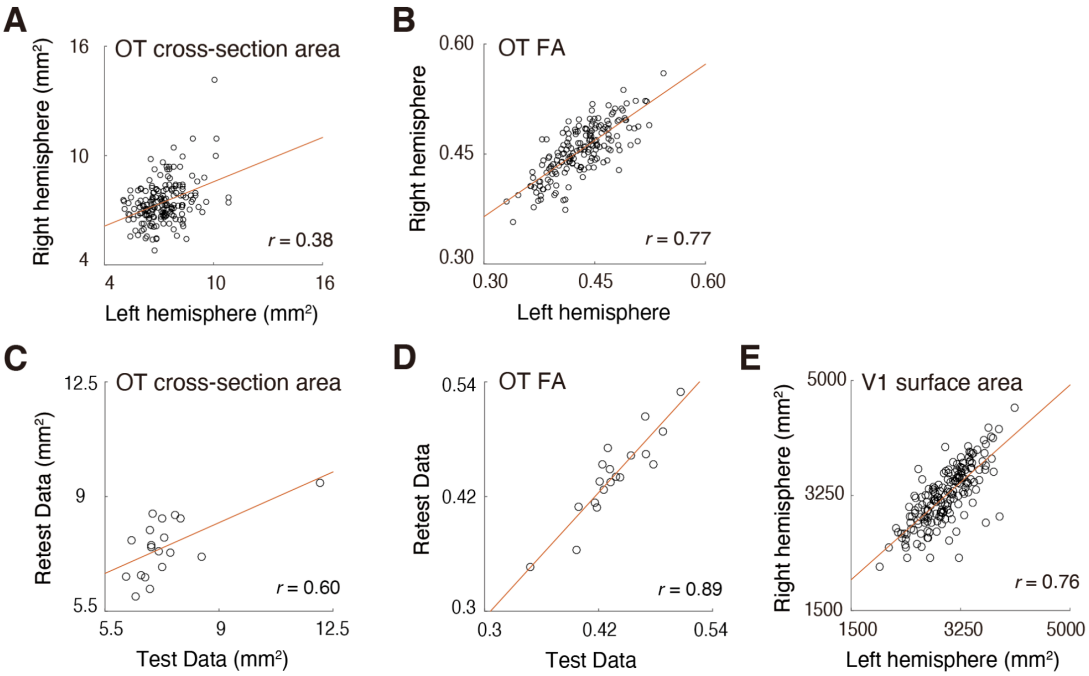

Figure 2.5. Assessment of reliability of OT measurements. A-B. Inter-hemispheric correlation of OT cross-section area (**A**) and OT FA (**B**). The OT cross-section area showed smaller inter-hemispheric correlation (r = 0.38) than OT FA (r = 0.77), presumably because of instability of dMRI-based measurements on the OT size. **C**. A scatter plot comparing OT cross-section area between test (horizontal axis) and retest data (vertical axis) acquired from the same subject (n = 19). **D**. A scatter plot comparing OT FA between test and retest dataset. **E**. Inter-hemispheric correlation of V1 surface area. Red lines in each plot indicate a linear regression line.

2.3.2 Correlation between V1 surface area and OT tissue properties

I investigated the correlation between V1 surface area and OT FA. Figure 2.6A depicts a scatter plot between these two quantities. I found a small, but statistically significant negative correlation between them (r = -0.19, P = 0.01), suggesting the existence of structural covariance between the surface area of V1 and tissue properties of the OT. The negative correlation was also observed when I performed a supplementary analysis separately analyzing data from the left and right hemisphere (r = -0.15 and -0.19 for left and right hemispheres, respectively).

I then asked whether this observed correlation in the main analysis, which used dMRI data acquired with b = 2,000 s/mm^2, generalizes. To this end, I performed the same analyses across different b-values (Lerma-Usabiaga et al., 2019). I found that the negative correlation between V1 surface area and OT FA is similar in other dMRI datasets with different acquisition parameters (Figure 2.6B; b = 1,000 s/mm^2, r = -0.15; b = 3,000 s/mm^2, r = -0.20). This result suggests that the observed structural covariance between V1 and OT FA is unlikely to be due to measurement noise.

The HCP 7T Retinotopy dataset includes many twin subjects (see subchapter 2.2 “Materials and Methods”) and twin pair subjects may show similar properties in OT and V1. I evaluated how much the inclusion of twin pairs in the dataset impacted the correlation between OT FA and V1 surface area. First, I randomly sampled 94 subjects from the whole dataset while avoiding the inclusion of twin pairs (for both MZ and DZ twins). I repeated this sampling procedure to generate many subsamples (see subchapter 2.2 “Materials and Methods”). Then for each subsample I calculated the correlation coefficient between OT FA and V1 surface area (blue in Figure 2.6C). The median correlation coefficient among subsamples was -0.21, which is comparable to that obtained in the main analysis of data from all subjects (Figure 2.6A). The distribution of correlation coefficients among subsamples avoiding twin pairs (blue in Figure 2.6C) significantly differs from the distribution of correlation coefficients when randomly shuffling the association between OT FA and V1 surface area (orange in Figure 2.6C). This result suggests that a negative correlation in OT FA and V1 surface area (Figure 2.6A) is preserved after excluding the impact of twin pairs.

I also investigated whether V1’s observed structural covariance with OT generalized to the other visual white matter tract. To this end, I identified the OR (Figure 2.7A), which is a geniculo-cortical pathway connecting the LGN and V1, from the dMRI dataset. I did not find a significant correlation between OR FA and V1 surface area, unlike with the OT (Figure 2.7B; r = 0.04, P = 0.61). I also did not find a significant correlation between OR FA and V1 surface area when I separately analyzed each hemisphere (r = 0.002 and 0.07 for left and right hemisphere, respectively).

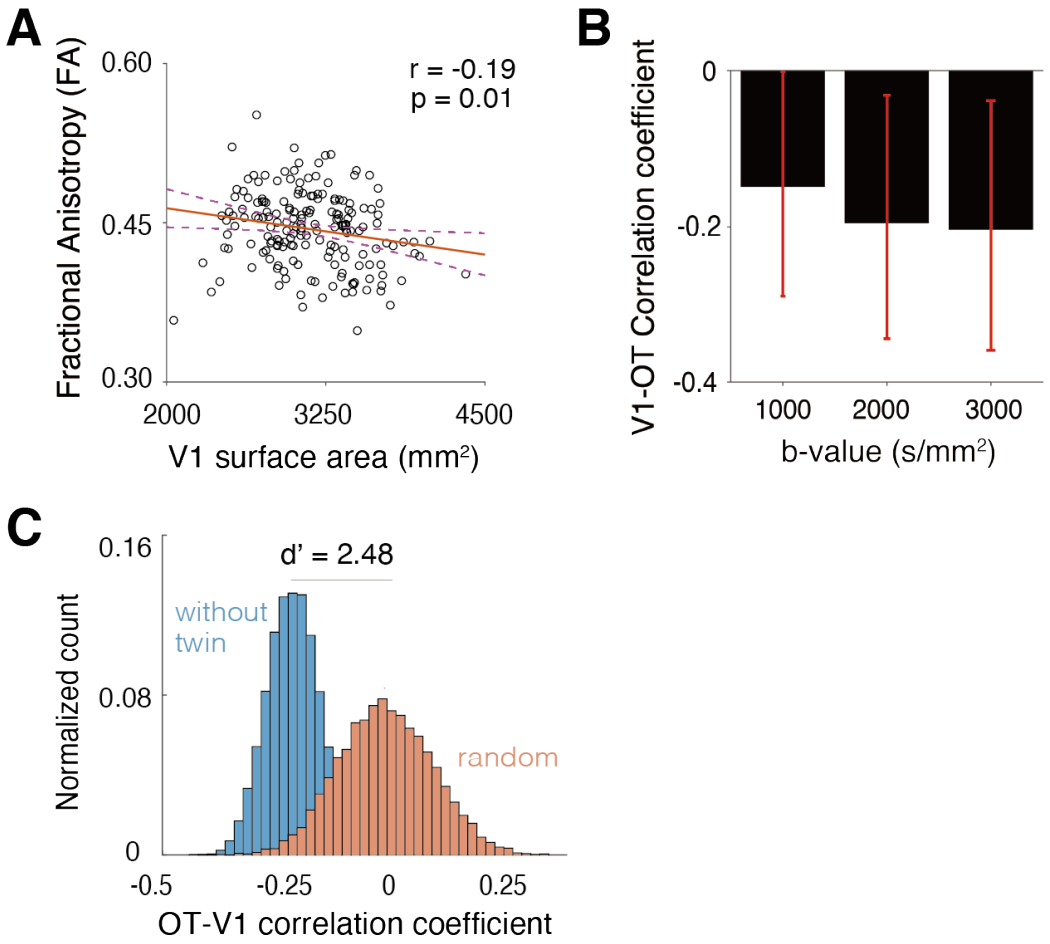

Figure 2.6. The correlation between V1 surface area and OT tissue property. A. A scatter plot of the V1 surface area (horizontal axis) and OT FA (vertical axis). The correlation between V1 surface area and FA along the OT was small, but statistically significant (r = -0.19, P = 0.009, N = 178). A red line indicates a linear regression line. The purple dotted curves indicate 95% confidence interval of a linear regression estimated by the bootstrapping. **B.** The correlation between V1 surface area and FA along the OT was replicated in dMRI data acquired with different b-values (b=1000 s/mm^2, weaker diffusion weighting; b=3000 s/mm^2, stronger diffusion weighting). The vertical axis depicts the correlation coefficient between V1 surface area and OT FA. I performed the bootstrap 10,000 times for each b-value to compute the 95% confidence interval of this probability. Error bars indicate this interval. **C**. Assessment of OT-V1 correlation when excluding twin subjects. The blue histogram indicates the probability density of the correlation coefficient between V1 surface area and OT fractional anisotropy (FA) when subsampling 94 subjects' data by avoiding the inclusion of both members of any twin pair. The red histogram shows the correlation coefficient when subsampling 178 subjects and shuffling the association between V1 surface area and OT FA. This histogram indicates that even if I exclude the effect of twin pairs (blue), the median correlation coefficient is almost equal to that of the main analysis (r = -0.21), and the distribution is clearly separate from that of random shuffling (d' = 2.48). The vertical axis of the histogram depicts the normalized count of correlation coefficient (from all shuffles), and the horizontal axis depicts the correlation coefficient between OT FA and V1 surface area.

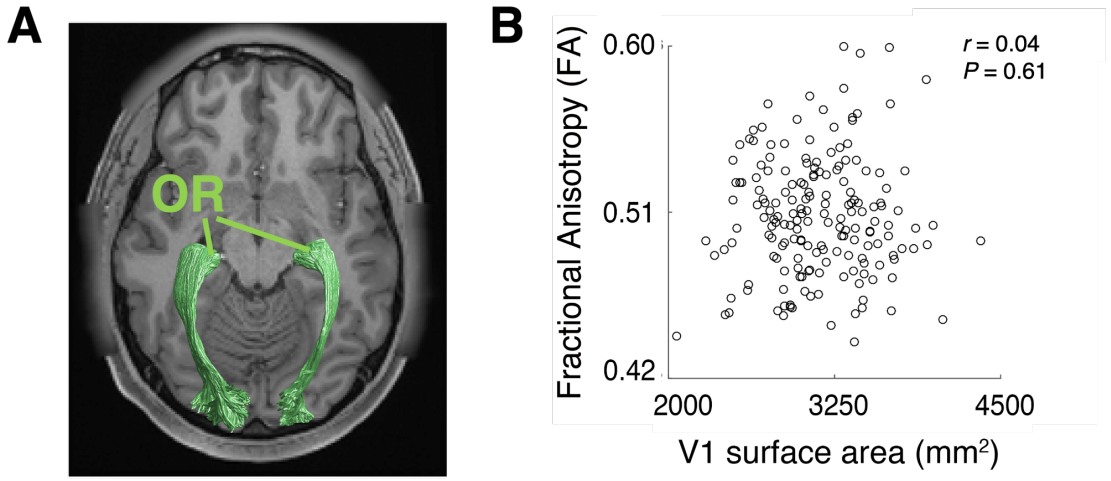

Figure 2.7. The correlation between V1 surface area and FA along the optic radiation (OR). A. The OR identified in a representative subject overlaid on an axial slice of the subject's T1-weighted image. **B**. Scatter plot comparing V1 surface area (horizontal axis) and OR FA (vertical axis). There was no significant correlation between V1 surface area and OR FA.

2.3.3 Possible microstructural basis of OT-V1 correlation evaluated by NODDI

While FA is a widely used metric with high reproducibility, it is based on a simplistic diffusion tensor model, and the interpretation of its microstructural origin is inherently ambiguous. To better understand the microstructural basis of the OT-V1 correlation, I used NODDI (Zhang et al., 2012), which is a multi-compartment model of dMRI data. NODDI enables one to estimate ICVF and ODI, which are thought to be correlated with neurite density and the orientation dispersion of fibers, respectively. Similar to FA, these metrics are strongly correlated between hemispheres (Figure 2.8A; ICVF, $r = 0.80$; Figure 2.8B; ODI, $r = 0.85$), suggesting high measurement reliability.

Figure 2.8 depicts scatter plots comparing V1 surface area and OT ICVF and ODI. I found a small, but statistically significant positive correlation with V1 surface area in both ICVF (Figure 2.8C; $r = 0.19$, $P = 0.01$) and ODI (Figure 2.8D; $r = 0.22$, $P = 0.003$). This result suggests that a negative correlation between FA and V1 surface area can be explained by greater axonal density and orientation dispersion in subjects with a larger V1 (Figure 2.8E; see "Microstructural origin of OT-V1 correlation" in the subchapter 2.4 "Discussion").

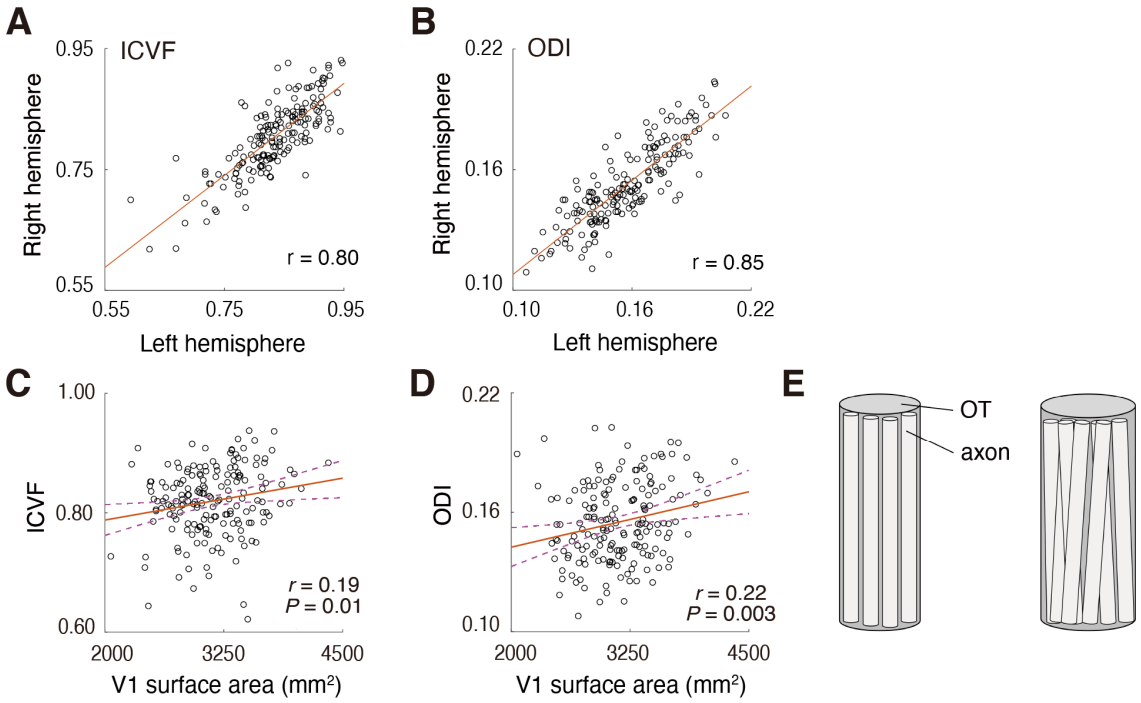

Figure 2.8. The correlation between V1 and NODDI properties. Inter-hemispheric correlation of OT ICVF (**A**) and OT ODI (**B**). There were positive correlations between V1 surface area and microstructural properties of the OT as quantified by NODDI (**C.** ICVF; **D.** ODI). Other conventions are identical to those used in Figure 2.6A. **E**. Schematic figure explaining how the number and the spatial configuration of axons correlates with V1 surface area. The pattern of OT-V1 correlation raises the hypothesis that individuals with smaller V1 surface areas have fewer axons and reduced orientation dispersion (left panel) relative to individuals with larger V1 surface areas (right panel).

2.3.4 Evaluating the impact of SNR of the MRI image

I further investigated how the SNR of the MRI image may contribute to the observed correlation between V1 surface area and OT measurements. To this end, I quantified SNR of b = 0 image within the OT in each individual subject and quantified the correlation between SNR and each OT measurement (Figure 2.9; cross-section area, FA, ICVF, and ODI). Three of the metrics do not show significant correlation with SNR (r = 0.13, -0.02, and -0.07; P = 0.08, 0.81, and 0.33 for cross-section area, FA, and ODI); therefore, it is not very likely that SNR variability across individuals explains correlations related to these metrics. In contrast, OT ICVF showed significant correlation with SNR (r = -0.24; P = 0.0001).

To control the influence of SNR on OT ICVF, I calculated a partial correlation between V1 surface area and OT ICVF with the effect of SNR removed. I still observe a positive correlation similar to the main analysis (r = 0.16). Therefore, I think that an inter-individual variability of SNR will not fully explain a positive correlation between V1 surface area and OT ICVF.

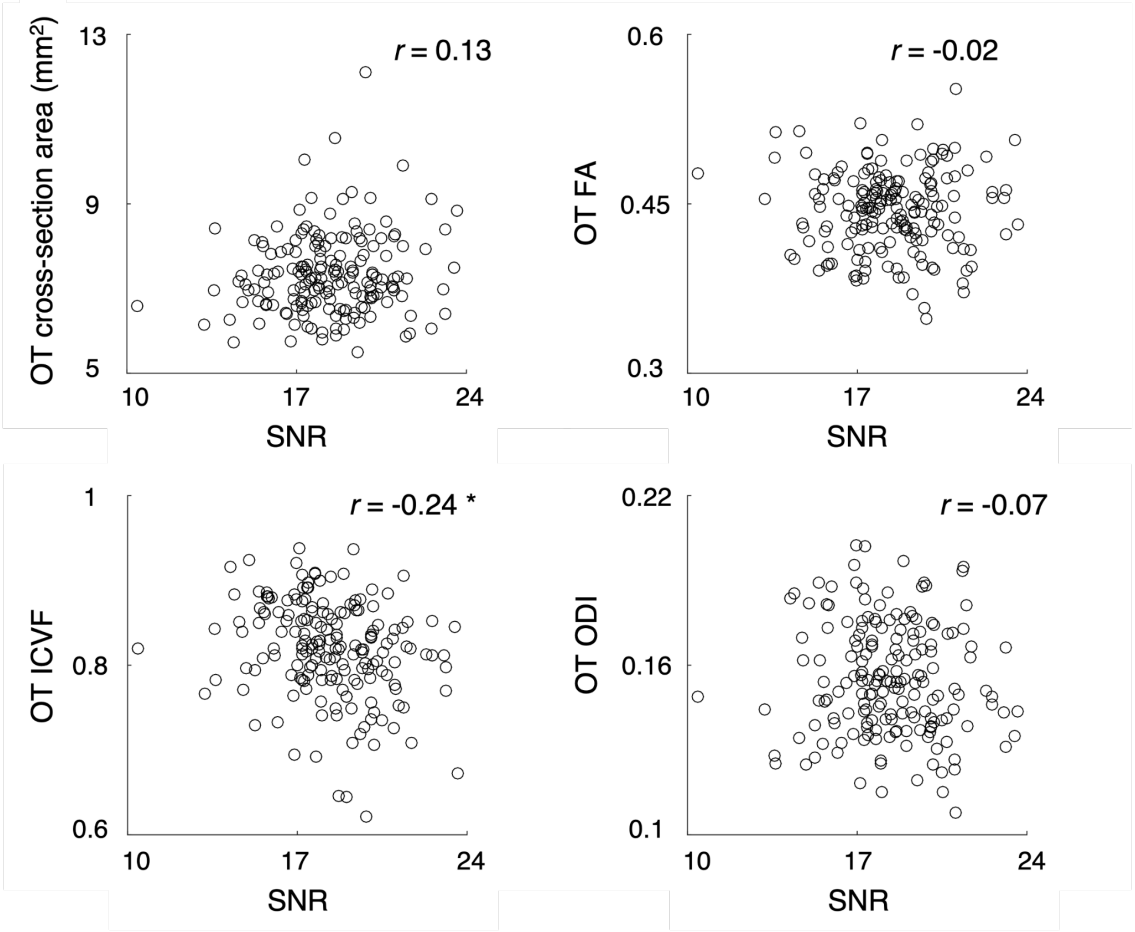

Figure 2.9. Scatter plot comparing SNR of b = 0 image and OT metrics. The horizontal axis represents SNR of b = 0 image within the OT. The vertical axis in each panel represents the OT measurements (left top panel, OT cross-section area; right top panel, OT FA; left bottom panel, OT ICVF; right bottom panel, OT ODI). Only OT ICVF showed statistically significant correlation (r = 0.24; P = 0.0001).

2.3.5 Heritability of human OT and V1 structural properties

Finally, I evaluated the heritability of OT FA and V1 surface area to understand whether individual variability of these measurements derives from genetic factors. To this end, I evaluated the correlation of OT FA and V1 surface areas between MZ and DZ twin pairs and calculated the heritability index (Falconer & Mackay, 1996). For both V1 surface area and OT FA, correlations between MZ twins were higher than correlations between DZ twins, suggesting a considerable degree of heritability (Figure 2.10A, Falconer's h^2 = 0.58 for OT FA; Figure 2.10B, Falconer's h^2 = 0.28 for V1 surface area; see Figure 2.10C-D for confidence intervals).

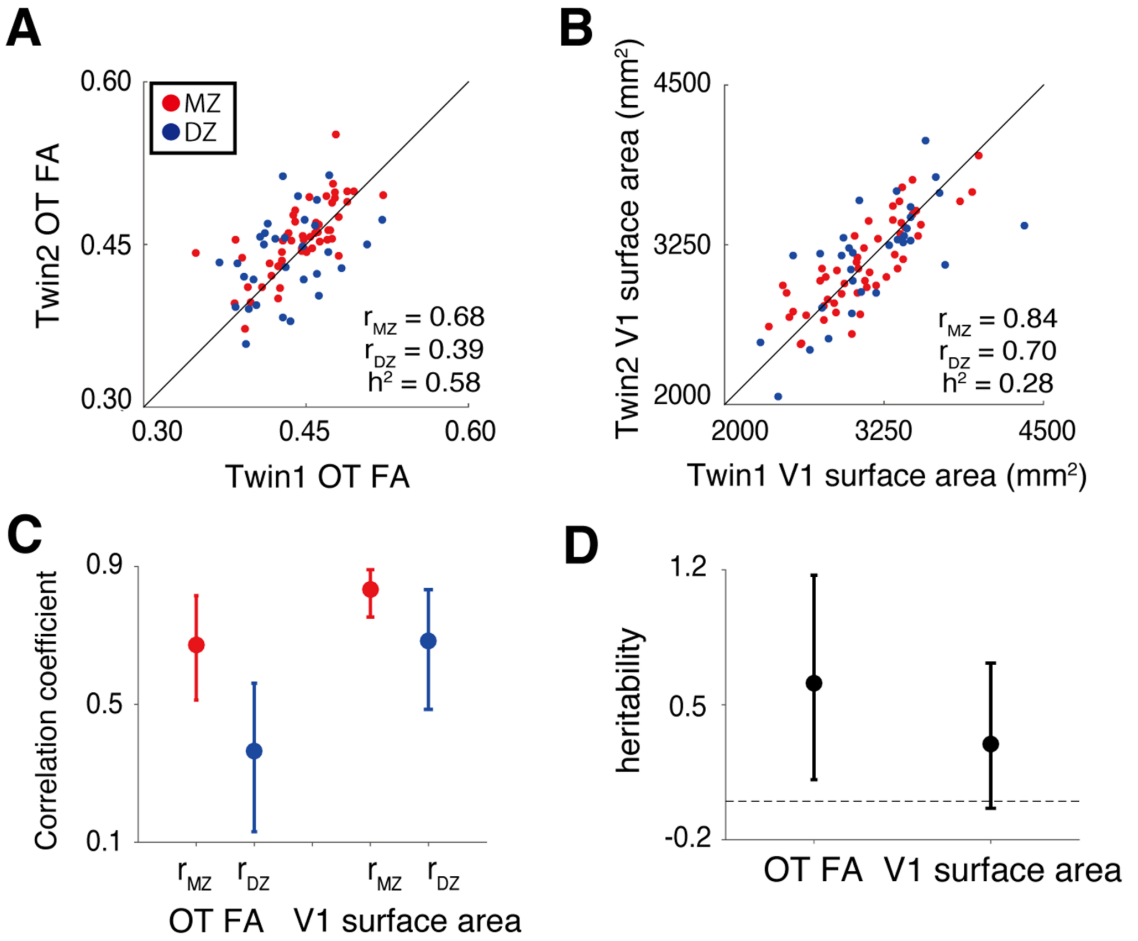

Figure 2.10. Heritability of structural properties of OT and V1 evaluated by analysis of twin data. The scatter plot depicts a comparison of twin pair data for OT FA (**A**) and V1 surface area (**B**). Red dots depict data from MZ twins whereas blue dots depict data from DZ twins. The black lines depict the line of equality (x = y). The heritability index (h^2) was calculated by Falconer's formula of heritability based on ICC in MZ and DZ data (r_{MZ} and r_{DZ}). **C**. Intraclass correlation coefficient (ICC) of OT FA and V1 surface area across monozygotic (MZ, red) and dizygotic (DZ, blue) twin pairs. **D.** Falconer's heritability index (vertical axis) of OT FA and V1 surface area. In both panels **C**, **D**, error bars depict the 95% confidence interval estimated using 10,000 bootstraps.

2.4 Discussion

I evaluated the structural covariance between V1 and OT in living humans, which was hypothesized based on previous anatomical work (Andrews et al., 1997), by analyzing fMRI and dMRI data in the HCP 7T Retinotopy dataset. I did not find a significant correlation between OT size and V1 surface area, presumably due to the instability of the OT size measurements from the dMRI data (Figure 2.2). In contrast, I found a significant negative correlation between V1 surface area and OT FA, and this correlation generalized across acquisition parameters (Figure 2.6). Moreover, I found that a negative correlation between OT FA and V1 could be explained by individual differences in intracellular diffusivity and orientation dispersion along the OT (Figure 2.8). Finally, I found that there is a considerable degree of heritability in both OT FA and V1 surface area (Figure 2.10), suggesting that genetic factors influence both measurements.

2.4.1 Structural covariance between OT and V1 in living humans

In contrast to previous work (Andrews et al., 1997), I did not find a statistically significant correlation between OT cross-section area and V1 surface area (Figure 2.2). This is likely because the spatial resolution of dMRI data (voxel size; 1.25 mm isotropic) is not sufficient to robustly identify the cross-section area of the OT, which ranges from 5.1 to 11.3 mm^2 in post-mortem living brains (Andrews et al., 1997). If I assume that the OT cross-section area is comparable in the living human brain, the number of voxels covering OT in each coronal section should range from 3 to 7. Because the estimation of the OT cross-section area significantly depends on the spatial arrangement of voxels and partial voluming with neighboring tissues (Figure 2.4), it is likely that measurements of the OT cross-section area are unstable at this spatial resolution. In fact, I also found the inter-hemispheric correlation of the OT cross-section area measurements from dMRI data to be low (Figure 2.5A; $r = 0.38$), confirming that this measurement is unstable.

In contrast, OT FA can be reliably measured from this dataset because in the AFQ analysis pipelines, as used by Yeatman et al. (2012), the tract profile of FA was calculated by taking a weighted average where the weights were defined based on distance from the tract core (see subchapter 2.2 “Materials and Methods”). This procedure is known to be highly reliable in terms of test-retest reliability (Kruper et al., 2021) and has successfully identified OT tissue abnormalities in retinal disease patients (Ogawa et al., 2014; Takemura et al., 2019). In fact, my results show that the inter-hemispheric correlation of OT FA is higher than that of OT cross-section area, suggesting that this is a more reliable dMRI-based metric for OT structural properties (Figure 2.5B). Because OT FA is a reliable measurement and because the significant negative correlation between OT FA and V1 surface area (Figure 2.6A) has been generalized across acquisition parameters (Figure 2.6B), my results support the existence of structural covariance between the OT and V1 in living human brains.

2.4.2 Microstructural origin of OT-V1 correlation

FA is a fairly reproducible dMRI-based metric of white matter microstructure (Kruper et al., 2021), but it does not have a direct correlation with specific microstructural properties, such as the properties of axons and myelin (Wandell & Le, 2017; Assaf et al., 2019). Therefore, it is challenging to interpret the microstructural origin of the OT-V1 correlation solely from FA results (Figure 2.6A). One plausible hypothesis is that individuals with larger V1s have more RGCs, and therefore those individuals will have more neurons in V1, which will result in greater V1 surface area. In fact, this hypothesis is supported by a correspondence of radial field asymmetries between retina and cortex at the population level (Kupers et al., 2022). If this is the case, the OT-V1 correlation may suggest that OT microstructural properties measured by dMRI are related to the number of RGCs. This interpretation remains speculative at this point, because the HCP 7T Retinotopy dataset does not have a direct measurement of RGCs.

One might wonder why the correlation between OT FA and V1 is negative, rather than positive, if the basis of individual differences are derived from differences in numbers of RGCs. To clarify this point, I used NODDI (Zhang et al., 2012), which is a multi-compartment model providing ICVF and ODI, two properties that are hypothesized to be correlated with neurite density and orientation dispersion, respectively (Mollink et al., 2017; Schilling et al., 2017). I found that both ICVF and ODI along the OT showed a positive correlation with V1 surface area (Figure 2.8C and 2.8D). This result is consistent with the interpretation that individuals with larger V1 have larger neurite density with more dispersed fiber orientations along the OT. This suggests that individuals with more RGCs are likely to have a larger number of axons (which might result in larger neurite density/ICVF), but the configuration of axonal orientation in such individuals may also be more dispersed than that of individuals with fewer RGCs (Figure 2.8E). Regardless, this hypothesis requires further evaluation by anatomical studies, because the microstructural interpretation of NODDI has some degree of uncertainty (Jelescu et al., 2016). It is also known that there is substantial individual variation in acuity at the fovea and in cone density at the fovea (Curcio et al., 1987). An important open question is whether differences in OT properties and V1 surface area can be traced all the way back to the photoreceptor mosaic.

2.4.3 No evidence of correlation between OR and V1

I did not find a significant correlation between OR FA and V1 surface area (Figure 2.7B). This is counter-intuitive, because the OR includes axons that directly project to V1. I speculate that this lack of significance can be explained by the fact that the OR comprises heterogenous fiber populations. For example, it is known that the OR includes feedback axons from V1 to LGN (Ichida & Casagrande, 2002; Angelucci & Sainsbury, 2006). In addition, a recent anatomical study reported that axons from the pulvinar merge into the OR and follow a path similar to that of axons from the LGN (Takemura et al., 2020). Therefore, unlike the OT, in which all axons are feedforward axons from RGCs, feedforward axons can only explain a part of the variance in dMRI measurements along

the OR. Resolving this uncertainty requires further anatomical investigations into how different axonal populations are spatially organized within the OR.

2.4.4 Possible underlying mechanism of structural covariance between OT and V1

While it is difficult to identify the underlying mechanisms of the structural covariance between OT and V1, there are, at minimum, several possible interpretations. First, because the OT does not contain feedback axons from V1, it is natural to infer that the OT influences V1, but that V1 would not conversely influence the OT. Accordingly, one hypothesis is that the development of the OT affects the maturation of V1, resulting in a correlation between them. The second possibility is that a common genetic factor affects the development of both OT and V1, resulting in structural covariance, without a direct relationship between the OT and V1.

Although these two possibilities are not mutually exclusive, I investigated the twin data included in the HCP 7T Retinotopy Dataset to better interpret the structural covariance of the OT and V1. I found that MZ twin pairs had higher correlations than DZ twins (Figure 2.10) for both the OT FA and V1 surface area, suggesting a considerable degree of heritability in these measurements. While the specific genetic factors contributing to the structural covariance between the OT and V1 remain uncertain, these results suggest that one plausible source of that covariance is common genetic factors. An extension of this study, by combining developmental neuroimaging and transcriptomics (Natu et al., 2021), may provide a more precise understanding of the developmental and genetic mechanisms of the structural covariance between the OT and V1.

In conclusion, I found a small, but statistically significant correlation between OT microstructural properties and V1 surface area. This correlation generalized across datasets acquired with different parameters. These results support the existence of structural covariance between the OT and V1, as hypothesized from previous anatomical work (Andrews et al., 1997). Because both the OT and V1 have a considerable degree of heritability, one plausible source of the structural covariance might be common genetic factors.

Chapter 3. References

Amemiya K, Naito E, Takemura H (2021) Age dependency and lateralization in the three branches of the human superior longitudinal fasciculus. Cortex 139:116–133.

Amunts K, Malikovic A, Mohlberg H, Schormann T, Zilles K (2000) Brodmann's Areas 17 and 18 Brought into Stereotaxic Space—Where and How Variable? NeuroImage 11:66–84.

Andersson JLR, Skare S, Ashburner J (2003) How to correct susceptibility distortions in spin-echo echo-planar images: application to diffusion tensor imaging. Neuroimage 20:870–888.

Andersson JLR, Sotiropoulos SN (2016) An integrated approach to correction for off-resonance effects and subject movement in diffusion MR imaging. Neuroimage 125:1063–1078.

Andrews TJ, Halpern SD, Purves D (1997) Correlated size variations in human visual cortex, lateral geniculate nucleus, and optic tract. J Neurosci 17:2859–2868.

Angelucci A, Sainsbury K (2006) Contribution of feedforward thalamic afferents and corticogeniculate feedback to the spatial summation area of macaque V1 and LGN. J Comp Neurol 498:330–351.

Assaf Y, Basser PJ (2005) Composite hindered and restricted model of diffusion (CHARMED) MR imaging of the human brain. NeuroImage 27:48–58.

Assaf Y, Johansen-Berg H, Thiebaut de Schotten M (2019) The role of diffusion MRI in neuroscience. NMR Biomed 32:e3762.

Bandettini P, Wong E, Hinks R, Tikofsky R, Hyde J (1992) Time course EPI of human brain function during task activation. Magnetic Resonance in Medicine 25 390–397.

Basser PJ, Mattiello J, LeBihan D (1994a) Estimation of the effective self-diffusion tensor from the NMR spin echo. Journal of Magnetic Resonance Series B 103(3) 247–254.

Basser PJ, Mattiello J, LeBihan D (1994b) MR diffusion tensor spectroscopy and imaging. Biophysical Journal 66(1) 259–267.

Basser PJ, Pierpaoli C (1996) Microstructural and physiological features of tissues elucidated by quantitative-diffusion-tensor MRI. J Magn Reson B 111:209–219.

Behrens TEJ, Woolrich MW, Jenkinson M, Johansen-Berg H, Nunes RG, Clare S, Matthews PM, Brady JM, Smith SM (2003) Characterization and propagation of uncertainty in diffusion-weighted MR imaging. Magnetic Resonance in Medicine 50(5) 1077–1088.

Behrens TEJ, Berg HJ, Jbabdi S, Rushworth MFS, Woolrich MW (2007) Probabilistic diffusion tractography with multiple fibre orientations: What can we gain? NeuroImage 34:144–155.

Benson NC, Butt OH, Datta R, Radoeva PD, Brainard DH, Aguirre GK (2012) The retinotopic organization of striate cortex is well predicted by surface topology. Curr Biol 22:2081–2085.

Benson NC, Butt OH, Brainard DH, Aguirre GK (2014) Correction of distortion in flattened representations of the cortical surface allows prediction of V1-V3 functional organization from anatomy. PLoS Comput Biol 10:e1003538.

Benson NC, Winawer J (2018) Bayesian analysis of retinotopic maps. Elife 7: e40224.

Benson N, Jamison K, Vu A, Winawer J, Kay K (2018) The HCP 7T Retinotopy Dataset: A new resource for investigating the organization of human visual cortex. Journal of Vision 18:215.

Benson NC, Yoon JMD, Forenzo D, Engel SA, Kay KN, Winawer J (2020) Variability of the Surface Area of the V1, V2, and V3 Maps in a Large Sample of Human Observers. bioRxiv 2020.12.30.424856.

Benson NC, Kupers ER, Barbot A, Carrasco M, Winawer J (2021) Cortical magnification in human visual cortex parallels task performance around the visual field. Elife 10: e67685.

Bergmann J, Genç E, Kohler A, Singer W, Pearson J (2016) Smaller Primary Visual Cortex Is Associated with Stronger, but Less Precise Mental Imagery. Cereb Cortex 26:3838–3850.

Bullock TH, Bennett MV, Johnston D, Josephson R, Marder E, Fields RD (2005) Neuroscience. The neuron doctrine, redux. Science 310(5749) 791–793.

Catani M, ffytche DH (2005) The rises and falls of disconnection syndromes. Brain : a journal of neurology 128(10) 2224–2239.

Conturo TE, Lori NF, Cull TS, Akbudak E, Snyder AZ, Shimony JS, McKinstry RC, Burton H, Raichle ME (1999) Tracking neuronal fiber pathways in the living human brain. Proceedings of the National Academy of Sciences of the United States of America 96(18) 10422–10427.

Curcio CA, Sloan KR, Packer O, Hendrickson AE, Kalina RE (1987) Distribution of Cones in Human and Monkey Retina: Individual Variability and Radial Asymmetry. Science 236:579–582.

DeYoe EA, Carman GJ, Bandettini P, Glickman S, Wieser J, Cox R, Miller D, Neitz J (1996) Mapping striate and extrastriate visual areas in human cerebral cortex. Proceedings of the National Academy of Sciences of the United States of America 93(6) 2382–2386.

Dougherty RF, Koch VM, Brewer AA, Fischer B, Modersitzki J, Wandell BA (2003) Visual field representations and locations of visual areas V1/2/3 in human visual cortex. J Vis 3(10): 586–598.

Duan Y, Norcia AM, Yeatman JD, Mezer A (2015) The Structural Properties of Major White Matter Tracts in Strabismic Amblyopia. Invest Ophthalmol Vis Sci 56:5152–5160.

Dumoulin SO, Wandell BA (2008) Population receptive field estimates in human visual cortex. Neuroimage 39:647–660.

Duncan RO, Boynton GM (2003) Cortical magnification within human primary visual cortex correlates with acuity thresholds. Neuron 38:659–671.

Edelstein WA, Hutchison JM, Johnson G, Redpath T (1980) Spin warp NMR imaging and applications to human whole-body imaging. Physics in medicine and biology 25(4) 751–756.

Engel SA, Glover GH, Wandell BA (1997) Retinotopic organization in human visual cortex and the spatial precision of functional MRI. Cerebral Cortex 7(2) 181–192.

Falconer DS, Mackay TFC (1996) Introduction to Quantitative Genetics, Ed 4. Harlow, Essex, UK.: Longmans Green.

Fields RD (2008) White matter matters. Scientific American 298(3) 42–49.

Fischl B (2012) FreeSurfer. Neuroimage 62:774–781.

Felleman DJ, Van Essen DC (1991) Distributed hierarchical processing in the primate cerebral cortex. Cerebral Cortex 1(1) 1–47.

Garroway AN, Grannell PK, Mansfield P (1974) Image Formation in NMR by a Selective Irradiative Process. J Phys C7:L457-462.

Genç E, Bergmann J, Singer W, Kohler A (2015) Surface area of early visual cortex predicts individual speed of traveling waves during binocular rivalry. Cereb Cortex 25:1499–1508.

Glasser MF, Sotiropoulos SN, Wilson JA, Coalson TS, Fischl B, Andersson JL, Xu J, Jbabdi S, Webster M, Polimeni JR, Van Essen DC, Jenkinson M, Consortium, W. U-Minn HCP (2013) The minimal preprocessing pipelines for the Human Connectome Project. Neuroimage 80:105–124.

Grill-Spector K, Kushnir T, Hendler T, Edelman S, Itzchak Y, Malach R (1998) A sequence of object-processing stages revealed by fMRI in the human occipital lobe. Human brain mapping 6(4) 316–328.

Hawken MJ, Parker AJ, Lund JS (1988) Laminar organization and contrast sensitivity of direction-selective cells in the striate cortex of the Old World monkey. The Journal of neuroscience 8(10) 3541–3548.

Henschen SE (1893) On the visual path and centre. Brain 16(1–2) 170–180.

Himmelberg MM, Winawer J, Carrasco M (2022) Linking individual differences in human primary visual cortex to contrast sensitivity around the visual field. bioRxiv:2021.10.04.463138.

Holmes G (1918) Disturbances of vision by cerebral lesions. British Journal of Ophthalmology 2 353–384.

Hubel DH, Wiesel TN (1962) Receptive fields, binocular interaction and functional architecture in the cat's visual cortex. J Physiol 160:106–154.

Huettel SA, Song AW, McCarthy G (Eds.) (2014) Functional Magnetic Resonance Imaging (3rd edition). Oxford university press.

Huk AC, Ress D, Heeger DJ (2001) Neuronal basis of the motion aftereffect reconsidered. Neuron 32(1) 161–172.

Ichida JM, Casagrande VA (2002) Organization of the feedback pathway from striate cortex (V1) to the lateral geniculate nucleus (LGN) in the owl monkey (Aotus trivirgatus). J Comp Neurol 454:272–283.

Inouye T (1909) Die Sehsto¨rungen bei Schußverletzungen der kortikalen Sehspha¨re. Leipzig, Germany: W. Engelmann.

Jelescu IO, Veraart J, Fieremans E, Novikov DS (2016) Degeneracy in model parameter estimation for multi-compartmental diffusion in neuronal tissue. NMR Biomed 29:33–47.

Johnson BM, Miao M, Sadun AA (1987) Age-related decline of human optic nerve axon populations. Age 10:5–9.

Kapitány K, Négyessy L, Barsi Á (2013) Tomographic reconstruction of micro-vascular network in cerebral cortical samples. Biomechanica Hungarica 6(1).

Kida I, Ueguchi T, Matsuoka Y, Zhou K, Stemmer A, Porter D (2016) Comparison of Diffusion-Weighted Imaging in the Human Brain Using Readout-Segmented EPI and PROPELLER Turbo Spin Echo With Single-Shot EPI at 7 T MRI. Invest Radiol 51:435–439.

Kruper J, Yeatman JD, Richie-Halford A, Bloom D, Grotheer M, Caffarra S, Kiar G, Karipidis II, Roy E, Chandio BQ, Garyfallidis E, Rokem A (2021) Evaluating the reliability of human brain white matter tractometry. Aperture Neuro 1:1.

Kumar A, Welti D, Ernst RR (1975) NMR Fourier Zeugmatography. J Magn Reson 18: 69-83.

Kupers ER, Benson NC, Carrasco M, Winawer J (2022) Asymmetries around the visual field: From retina to cortex to behavior. PLoS Comput Biol 18: e1009771.

Kwong KK, Belliveau JW, Chesler DA, Goldberg IE, Weisskoff RM, Poncelet BP, Kennedy DN, Hoppel BE, Cohen MS, Turner R (1992) Dynamic magnetic resonance imaging of human brain activity during primary sensory stimulation. Proceedings of the National Academy of Sciences of the United States of America, 89, 5675–5679.

Lauterbur PC (1973) Image Formation by Local Induced Interactions: Examples Employing Nuclear Magnetic Resonance. Nature 242: 190-191.

Lebel C, Beaulieu C (2011) Longitudinal development of human brain wiring continues from childhood into adulthood. Journal of Neuroscience 31(30) 10937–10947.

Lebel C, Gee M, Camicioli R, Wieler M, Martin W, Beaulieu C (2012) Diffusion tensor imaging of white matter tract evolution over the lifespan. NeuroImage 60: 340–352.

LeBihan D, Breton E, Lallemand D, Grenier P, Cabanis E, Laval-Jeantet M (1986) MR imaging of intravoxel incoherent motions: application to diffusion and perfusion in neurologic disorders. Radiology 161(2) 401–407.

Lerma-Usabiaga G, Mukherjee P, Ren Z, Perry ML, Wandell BA (2019) Replication and generalization in applied neuroimaging. Neuroimage 202:116048.

Livingstone MS, Hubel DH (1984) Anatomy and physiology of a color system in the primate visual cortex. The Journal of neuroscience 4(1) 309–356.

Livingstone M, Hubel D (1988) Segregation of form, color, movement, and depth: anatomy, physiology, and perception. Science 240(4853) 740–749.

Mechelli A, Friston KJ, Frackowiak RS, Price CJ (2005) Structural covariance in the human cortex. J Neurosci 25:8303–8310.

Mollink J, Kleinnijenhuis M, van Cappellen van Walsum A-M, Sotiropoulos SN, Cottaar M, Mirfin C, Heinrich MP, Jenkinson M, Pallebage-Gamarallage M, Ansorge O, Jbabdi S, Miller KL (2017) Evaluating fibre orientation dispersion in white matter: Comparison of diffusion MRI, histology and polarized light imaging. Neuroimage 157:561–574.

Mori S, Crain BJ, Chacko VP, van Zijl PC (1999) Three-dimensional tracking of axonal projections in the brain by magnetic resonance imaging. Annals of Neurology, 45(2), 265–269.

Mori S, Zhang J (2006) Principles of diffusion tensor imaging and its applications to basic neuroscience research. Neuron 51(5) 527–539.

Natu VS, Rosenke M, Wu H, Querdasi FR, Kular H, Lopez-Alvarez N, Grotheer M, Berman S, Mezer AA, Grill-Spector K (2021) Infants' cortex undergoes microstructural growth coupled with myelination. Commun Biol. 4:1191.

Ogawa S, Lee TM (1990) Magnetic resonance imaging of blood vessels at high fields: In vivo and in vitro measurements and image simulation. Magnetic Resonance in Medicine 16(1) 9–18.

Ogawa S, Lee TM, Kay AR, Tank DW (1990) Brain magnetic resonance imaging with contrast dependent on blood oxygenation. Proceedings of the National Academy of Sciences of the United States of America 87(24) 9868–9872.

Ogawa S, Lee TM, Nayak AS, Glynn P (1990) Oxygenation-sensitive contrast in magnetic resonance image of rodent brain at high magnetic fields. Magnetic Resonance in Medicine 14(1) 68–78.

Ogawa S, Takemura H, Horiguchi H, Terao M, Haji T, Pestilli F, Yeatman JD, Tsuneoka H, Wandell BA, Masuda Y (2014) White matter consequences of retinal receptor and ganglion cell damage. Invest Ophthalmol Vis Sci 55:6976–6986.

Ogawa S, Tank D, Menon R, Ellermann J, Kim S, Merkle H, Ugurbil K (1992) Intrinsic signal changes accompanying sensory stimulation: Functional brain mapping with magnetic resonance imaging. Proceedings of the National Academy of Sciences of the United States of America 89 591–5955.

Ohzawa I, DeAngelis GC, Freeman RD (1990) Stereoscopic depth discrimination in the visual cortex: neurons ideally suited as disparity detectors. Science 249(4972) 1037–1041.

Purves D, Augustine GJ, Fitzpatrick D, Hall WC, LaMantia A-S, McNamara JO, White L E (Eds.) (2008) Neuroscience (4th edition). Sinauer Associates.

Raffelt D, Tournier J-D, Rose S, Ridgway GR, Henderson R, Crozier S, Salvado O, Connelly A (2012) Apparent Fibre Density: a novel measure for the analysis of diffusion-weighted magnetic resonance images. Neuroimage 59:3976–3994.

Reeder SB, Wintersperger BJ, Dietrich O, Lanz T, Greiser A, Reiser MF, Glazer GM, Schoenberg SO (2005) Practical approaches to the evaluation of signal-to-noise ratio performance with parallel imaging: Application with cardiac imaging and a 32-channel cardiac coil. Magnetic Resonance in Medicine 54:748–754.

Rockland KS (2020) What we can learn from the complex architecture of single axons. Brain structure & function 225(4) 1327–1347.

Rokem A, Takemura H, Bock AS, Scherf KS, Behrmann M, Wandell BA, Fine I, Bridge H, Pestilli F (2017) The visual white matter: The application of diffusion MRI and fiber tractography to vision science. J Vis 17(2):4.

Roland PE, Graufelds CJ, W Hlin J, Ingelman L, Andersson M, Ledberg A, Pedersen J, Akerman S, Dabringhaus A, Zilles K (1994) Human brain atlas: For high-resolution functional and anatomical mapping. Human brain mapping 1(3) 173–184.

Sanders MD, Warrington EK, Marshall J, Wieskrantz L (1974) "Blindsight": Vision in a field defect. Lancet (London, England) 1(7860) 707–708.

Schilling KG, Janve V, Gao Y, Stepniewska I, Landman BA, Anderson AW (2017) Histological validation of diffusion MRI fiber orientation distributions and dispersion. Neuroimage 165:200–221.

Schwarzkopf DS, Song C, Rees G (2011) The surface area of human V1 predicts the subjective experience of object size. Nat Neurosci 14:28–30.

Sereno MI, Dale AM, Reppas JB, Kwong KK, Belliveau JW, Brady TJ, Rosen BR, Tootell RB (1995) Borders of multiple visual areas in humans revealed by functional magnetic resonance imaging. Science 268(5212) 889–893.

Sherbondy AJ, Dougherty RF, Ben-Shachar M, Napel S, Wandell BA (2008) ConTrack: finding the most likely pathways between brain regions using diffusion tractography. J Vis 8(9):15.

Shrout PE, Fleiss JL (1979) Intraclass correlations: uses in assessing rater reliability. Psychol Bull 86:420–428.

Solomon SG, Lennie P (2007) The machinery of colour vision. Nature reviews. Neuroscience 8(4) 276–286.

Song C, Schwarzkopf DS, Rees G (2013) Variability in visual cortex size reflects tradeoff between local orientation sensitivity and global orientation modulation. Nat Commun 4:2201.

Song C, Schwarzkopf DS, Kanai R, Rees G (2015) Neural population tuning links visual cortical anatomy to human visual perception. Neuron 85:641–656.

Stensaas SS, Eddington DK, Dobelle WH (1974) The topography and variability of the primary visual cortex in man. J Neurosurg 40:747–755.

Takemura H, Ogawa S, Mezer AA, Horiguchi H, Miyazaki A, Matsumoto K, Shikishima K, Nakano T, Masuda Y (2019) Diffusivity and quantitative T1 profile of human visual white matter tracts after retinal ganglion cell damage. Neuroimage Clin 23:101826.

Takemura H, Palomero-Gallagher N, Axer M, Gräßel D, Jorgensen MJ, Woods R, Zilles K (2020) Anatomy of nerve fiber bundles at micrometer-resolution in the vervet monkey visual system. Elife 9: e55444.

Thiebaut de Schotten M, Dell'Acqua F, Forkel SJ, Simmons A, Vergani F, Murphy DG, Catani M (2011) A lateralized brain network for visuospatial attention. Nat Neurosci 14:1245–1246.

Tournier JD, Calamante F, Connelly A (2012) MRtrix: Diffusion tractography in crossing fiber regions. International Journal of Imaging Systems and Technology Volume 22 Issue 1 53-66.

Ungerleider LG, Mishkin M (1982) Two cortical visual systems. In Ingle DJ & Goodale MA & Mansfield RJW (Eds.) Analysis of visual behavior The MIT Press 549–586

Vu AT, Jamison K, Glasser MF, Smith SM, Coalson T, Moeller S, Auerbach EJ, Uğurbil K, Yacoub E (2017) Tradeoffs in pushing the spatial resolution of fMRI for the 7T Human Connectome Project. Neuroimage 154:23–32.

Van Essen DC, Anderson CH, Felleman DJ (1992) Information processing in the primate visual system: an integrated systems perspective. Science 255(5043) 419–423.

Van Essen DC, Ugurbil K, Auerbach E, Barch D, Behrens TEJ, Bucholz R, Chang A, Chen L, Corbetta M, Curtiss SW, Della Penna SD, Feinberg D, Glasser MF, Harel N, Heath AC, Larson-Prior L, Marcus D, Michalareas G, Moeller S, Oostenveld R, Petersen SE, Prior F, Schlaggar BL, Smith SM, Snyder AZ, Xu J, Yacoub E, WU- Minn HCP Consortium (2012) The Human Connectome Project: a data acquisition perspective. Neuroimage 62:2222–2231.

Van Essen DC, Smith SM, Barch DM, Behrens TEJ, Yacoub E, Ugurbil K, WU-Minn HCP Consortium (2013) The WU-Minn Human Connectome Project: an overview. Neuroimage 80:62–79.

Wandell BA (2016) Clarifying Human White Matter. Annual review of neuroscience 39 103–128.

Wandell BA, Winawer J (2011) Imaging retinotopic maps in the human brain. Vision Res 51:718–737.

Wandell BA, Le RK (2017) Diagnosing the Neural Circuitry of Reading. Neuron 96:298–311.

Wässle H, Boycott BB (1991) Functional architecture of the mammalian retina. Physiological reviews 71(2) 447–480.

Weiskrantz L, Warrington EK, Sanders MD, Marshall J (1974) Visual capacity in the hemianopic field following a restricted occipital ablation. Brain : a journal of neurology 97(4) 709–728.

Yeatman JD, Dougherty RF, Myall NJ, Wandell BA, Feldman HM (2012) Tract profiles of white matter properties: automating fiber-tract quantification. PLoS One 7:e49790.

Yeatman JD, Wandell BA, Mezer AA (2014) Lifespan maturation and degeneration of human brain white matter. Nature communications 5 4932.

Yendiki A, Panneck P, Srinivasan P, Stevens A, Zöllei L, Augustinack J, Wang R, Salat D, Ehrlich S, Behrens T, Jbabdi S, Gollub R, Fischl B (2011) Automated probabilistic reconstruction of white-matter pathways in health and disease using an atlas of the underlying anatomy. Frontiers in neuroinformatics 5 23.

Zhang H, Schneider T, Wheeler-Kingshott CA, Alexander DC (2012) NODDI: practical in vivo neurite orientation dispersion and density imaging of the human brain. Neuroimage 61:1000–1016.

Zilles K, Werners R, Büsching U, Schleicher A (1986) Ontogenesis of the laminar structure in areas 17 and 18 of the human visual cortex. A quantitative study. Anatomy and embryology 174(3) 339–353.

Zworykin VP (1980) Some new data on individual quantitative peculiarities of the human lateral geniculate body. Arch Anat Histol Embryol 3:27.

Chapter 4. Acknowledgement

I am grateful to Dr. Hiromasa Takemura for helpful support and suitable advice. He provided me with a basis of the MRI analysis and knowledge of the development of neuroimaging, large parts of the dissertation work. He also gave me advice not only for research but also for my life.

I am also thankful to Jonathan Winawer of NewYork University and Noah C Benson of University of Washington, collaborators of study written in this dissertation. They also provide me with excellent comments and suggestions.

I would like to express my gratitude to Dr. Shigeru Kitazawa for his continuous support, constructive advice and warm encouragement. He encouraged me to pursue my research interests through valuable advice and discussions.

I am also thankful to Dr. Toshio Yanagida for his kind support and advice. He also provides me with a wonderful research environment at CiNet.

I also thank Dr. Ichiro Fujita for his support and thoughtful guidance. He provides me with a great opportunity to study two-photon calcium imaging in the macaque visual cortex, which I am very interested in during my master degree.

I would like to thank Yusuke Sakai for his help in support of data curation and analysis.

I thank all of my prior and current members of my laboratory, CiNet, and Division of Sensory and Cognitive Brain Mapping (Takemura Lab) of National Institute for Physiological Sciences (NIPS), Okazaki. They gave me advice about studies and helped me with my daily things.

I would like to express my appreciation to Dr. Shinji Nishimoto, Dr. Takafumi Suzuki, and Dr. Hiroshi Ban for serving the dissertation committee.

Finally, I would like to thank my family for a lot of support and encouragement.

Chapter 5. Achievements

Peer Review Journal Articles

Miyata, T., Benson, N.C., Winawer, J. & Takemura, H. (2022) Structural covariance and heritability of the optic tract and primary visual cortex in living human brains. *The Journal of Neuroscience*, 42, 6761-6769.

International conferences

Poster presentation

Miyata, T., Benson, N.C., Winawer, J. & Takemura, H. Investigating structural covariance of the human optic tract and primary visual cortex in a neuroimaging dataset. Society for Neuroscience Global Connectome, P192.01. (2021, January)

Miyata, T., Benson, N.C., Winawer, J. & Takemura, H. Structural covariance and heritability of the optic tract and primary visual cortex in living human. Organization for Human Brain Mapping annual meeting, #1456. (2021, June)

Miyata, T., Benson, N.C., Winawer, J. & Takemura, H. Correlation between microstructural properties of the optic tract and size of primary visual cortex. Organization for Human Brain Mapping annual meeting, #MT1015, Glasgow, Scotland. (2022, June)

Domestic conference

Oral presentation

宮田季和, Noah C. Benson, Jonathan Winawer, 竹村浩昌. 機能的 MRI および拡散強調 MRI を用いたヒト一次視覚野表面積と視索の関連の検討. 日本視覚学会 2021 年冬季大会, 1o06. (2021, 1 月)

宮田季和, Noah C. Benson, Jonathan Winawer, 竹村浩昌. Assesing structural covariance of primary visual cortex in a neuroimaging dataset. 第 5 回ヒト脳イメージング研究会. (2021, 9 月)

Poster presentation

宮田季和, Noah C. Benson, Jonathan Winawer, 竹村浩昌. Structural covariance and heritability of primary visual cortex and white matter tract in neuroimaging dataset. The 7th CiNet Conference, #3-4. (2022, 2 月)